

RESEARCH ARTICLE

Tethered balloon measurements reveal enhanced aerosol occurrence aloft interacting with Arctic low-level clouds

Christian Pilz^{1,*}, John J. Cassano^{2,3,4}, Gijs de Boer^{3,5}, Benjamin Kirbus⁶, Michael Lonardi⁶, Mira Pöhlker¹, Matthew D. Shupe^{3,5}, Holger Siebert¹, Manfred Wendisch⁶, and Birgit Wehner¹

Low-level clouds in the Arctic affect the surface energy budget and vertical transport of heat and moisture. The limited availability of cloud-droplet-forming aerosol particles strongly impacts cloud properties and lifetime. Vertical particle distributions are required to study aerosol-cloud interaction over sea ice comprehensively. This article presents vertically resolved measurements of aerosol particle number concentrations and sizes using tethered balloons. The data were collected during the Multidisciplinary drifting Observatory for the Study of Arctic Climate expedition in the summer of 2020. Thirty-four profiles of aerosol particle number concentration were observed in 2 particle size ranges: 12-150 nm (N_{12-150}) and above 150 nm $(N_{>150})$. Concurrent balloon-borne meteorological measurements provided context for the continuous profiles through the cloudy atmospheric boundary layer. Radiosoundings, cloud remote sensing data, and 5-day back trajectories supplemented the analysis. The majority of aerosol profiles showed more particles above the lowest temperature inversion, on average, double the number concentration compared to below. Increased N_{12-150} up to 3,000 cm⁻³ were observed in the free troposphere above low-level clouds related to secondary particle formation. Long-range transport of pollution increased $N_{>150}$ to 310 cm⁻³ in a warm, moist air mass. Droplet activation inside clouds caused reductions of $N_{>150}$ by up to 100%, while the decrease in N_{12-150} was less than 50%. When low-level clouds were thermodynamically coupled with the surface, profiles showed 5 times higher values of N_{12-150} in the free troposphere than below the cloud-capping temperature inversion. Enhanced N_{12-150} and $N_{>150}$ interacting with clouds were advected above the lowest inversion from beyond the sea ice edge when clouds were decoupled from the surface. Vertically discontinuous aerosol profiles below decoupled clouds suggest that particles emitted at the surface are not transported to clouds in these conditions. It is concluded that the cloud-surface coupling state and free tropospheric particle abundance are crucial when assessing the aerosol budget for Arctic low-level clouds over sea ice.

Keywords: Arctic, Aerosols, Vertical distribution, Atmospheric boundary layer, Clouds, Tethered balloon, MOSAiC

1. Introduction

The Arctic responds in an amplified way to global warming. Between 1979 and 2021, the Arctic mean near-surface air temperature increased 3–4 times faster than the global mean (Rantanen et al., 2022) due to local and remote processes and feedback mechanisms (Serreze and Barry, 2011; Overland et al., 2015; Wendisch et al., 2023a). The

troposphere plays an impactful role in the Arctic climate system by interacting with the ocean and sea ice (Rinke et al., 2019). Commonly, prevailing low-level clouds, in particular in summer, affect the turbulent transport of heat and moisture (Brooks et al., 2017; Chechin et al., 2023), and the surface energy budget via cloud radiative forcing (Shupe and Intrieri, 2004). The limited number of

¹Atmospheric Microphysics Department, Leibniz Institute for Tropospheric Research (TROPOS), Leipzig, Germany

²National Snow and Ice Data Center (NSIDC), University of Colorado Boulder, Boulder, CO, USA

³Cooperative Institute for Research in Environmental Sciences (CIRES), University of Colorado, Boulder, CO, USA

⁴Department of Atmospheric and Oceanic Sciences, University of Colorado Boulder, Boulder, CO, USA

⁵Physical Sciences Laboratory (PSL), National Oceanic and Atmospheric Administration (NOAA), Boulder, CO, USA

⁶Leipzig Institute for Meteorology (LIM), Leipzig University, Leipzig, Germany

^{*}Corresponding author:

aerosol particles acting as cloud condensation nuclei (CCN) strongly influences cloud microphysics and, thus, the cloud radiative properties (Becker et al., 2023; Wendisch et al., 2023b) and lifetime (Lubin and Vogelmann, 2006; Mauritsen et al., 2011; Morrison et al., 2012).

Aerosol properties and abundance in the sea-icecovered central Arctic were mainly studied via shipbased observations during multiple icebreaker campaigns (Heintzenberg and Leck, 2012). Results have consistently shown that the particle number size distribution (PNSD) in summer is dominated by nucleation and Aitken mode particles with a lower contribution of accumulation mode particles (Heintzenberg et al., 2015; Boyer et al., 2023). The nucleation and Aitken mode particles mainly stem from secondary particle formation, which form from precursor gases from marine biogenic emissions (Kecorius et al., 2019) or iodic acid related to the freeze-up in late summer (Baccarini et al., 2018). Due to commonly high supersaturation conditions in Arctic low-level clouds (Leaitch et al., 2016), particles can be activated to CCN at sizes below 50 nm (Baccarini et al., 2018; Kecorius et al., 2019; Karlsson et al., 2021). Subsequent cloud processing supports particle growth and the release of accumulation mode particles when droplets evaporate, thus resulting in a bimodal PNSD (Hoppel et al., 1994), which comprises another characteristic of the central Arctic in summer (Boyer et al., 2023). Primarily emitted marine biogenic particles from the marginal sea ice zone or open leads contribute comparably low particle numbers (Held et al., 2011) that can contribute to the Aitken (Lawler et al., 2021) and accumulation mode (Heintzenberg and Leck, 2012).

Rare airborne observations in the central Arctic have provided some key information on aerosol sources and properties vertically (Abbatt et al., 2019; Wendisch et al., 2019; Willis et al., 2019; Wendisch et al., 2021). Secondary particle formation was observed close to the surface in relation to biogenic precursor gas emissions from open leads, the marginal sea ice zone, open ocean, or coastal regions in summer (Kupiszewski et al., 2013; Willis et al., 2016; Burkart et al., 2017; Willis et al., 2017). In contrast, a recent modeling study by Price et al. (2023), based on the measurements by Kupiszewski et al. (2013), emphasized the importance of a free tropospheric source of Aitken mode particles from secondary formation. Long-range pollution transport was only observed at higher altitudes with a low potential to be mixed to the surface due to slow large-scale subsidence of air masses (Kupiszewski et al., 2013). However, the aircraft and helicopter-borne measurements were mainly conducted outside low-level clouds and provided coarse vertical resolutions, thus limiting their representativeness for the lower troposphere. In particular, because the lower troposphere is commonly complexly structured, showing multiple temperature inversions and frequent low-level clouds (Tjernström and Graversen, 2009; Brooks et al., 2017).

In the neutrally stratified atmospheric boundary layer above the sea ice in summer, turbulence is induced by cloud-top radiative cooling aloft and wind shear at the surface (Brooks et al., 2017). When the cloud-driven turbulence extends sufficiently downward to connect with the surfacemixed layer, cloud-surface coupling results in continuous mixing up to the base of the lowest temperature inversion at the cloud-top region. In turn, discontinuous mixing occurs in decoupled cases when the cloud-mixed layer (CML) and the surface-mixed layer are separated by a temperature inversion below the cloud base. Thus, surface-based aerosol measurements may not represent particle properties in the cloud layer in decoupled cases (Shupe et al., 2013). Observations and modeling studies showed that cloud-top entrainment of moisture from above the inversion could sustain the cloud lifetime (Solomon et al., 2011; Egerer et al., 2021a). Similarly, aerosol particles could possibly be mixed down (Igel et al., 2017) or get activated as CCN when the cloud top extends into the temperature inversion (Sedlar et al., 2012). However, a comprehensive database of particle number concentration profiles through Arctic low-level clouds to explore the relevance of free tropospheric aerosols for the CCN budget and the near-surface abundance is not available.

In this article, we report on tethered balloon-borne measurements made during the Multidisciplinary drifting Observatory for the Study of Arctic Climate (MOSAiC) expedition in the summer of 2020 (Shupe et al., 2022; Lonardi et al., 2023). The balloon-borne modular utility for profiling the lower atmosphere (BELUGA; Egerer et al. 2019) was deployed from an ice floe drifting in the Fram Strait (Pilz et al., 2023) supported by the German icebreaking research vessel (RV) Polarstern (Knust, 2017). The advantage of BELUGA in providing high-resolution observations through low-level Arctic clouds above sea ice was previously demonstrated during the PASCAL (Physical Feedbacks of Arctic Boundary Layer, Sea Ice, Cloud and Aerosol) campaign (Egerer et al., 2019; Wendisch et al., 2019). Lonardi et al. (2022a) gave an overview of the BELUGA measurements during MOSAiC, highlighting the interconnections between atmospheric boundary layer structure, turbulence, radiation, and aerosol particle abundance.

This study focuses on 34 profiles of particle number concentration in the size range from 12 to 150 nm (N_{12-150}) and above 150 nm $(N_{>150})$. The impact of aerosol sources and sinks and the thermodynamic structure of the lower troposphere on the vertical particle abundance is evaluated. Parallel meteorological observations carried out with instruments attached to the balloon in combination with cloud remote sensing are used to determine the tropospheric structure during the aerosol observations. The effect of air mass origin and history is analyzed with 5-day back trajectories to derive vertically resolved aerosol transport patterns and the effect of air mass advection over sea ice on the tropospheric structure. Example profiles are used to explore possible particle processes in detail. Summarized particle number concentration profiles are derived for commonly observed lower tropospheric structures.

2. Methods

2.1. Tethered balloon deployments during the expedition

During the summer part of MOSAiC, the tethered balloon system BELUGA (Egerer et al., 2019) was deployed from

the ice floe about 260 m away from RV Polarstern between June 29 and July 27, 2020 (Lonardi et al., 2022a; Pilz et al., 2023). For the time of the BELUGA operations, RV Polarstern drifted with the ice floe from the Arctic Ocean at 82.2°N, 10.1°E into the Greenland Sea at 79.1°N, 2.4°W (Figure S1), serving as the base of operations for a wide range of additional observations of the atmosphere, sea ice, and ocean (Shupe et al., 2022). A 90 m³ tethered balloon carried 5 instrument packages in varying configurations from the sea ice surface up to an average maximum altitude of 1 km. The profile observations below, inside, and above clouds were conducted at an average ascent/descent rate of 0.5 m s⁻¹ at surface wind speeds below 7.5 m s⁻¹. This study focuses on simultaneous aerosol and meteorological observations of 34 profiles (ascent and descent) obtained from 17 flights over 14 days.

2.2. Balloon-borne aerosol measurements

The aerosol profile observations with BELUGA were made with the cubic aerosol measurement platform (CAMP), which is described in detail by Pilz et al. (2022a). This study focuses on observations by a condensation particle counter (CPC; modified model 3007, TSI Inc., USA) and a portable optical particle spectrometer (POPS; Handix Scientific, USA). The CPC measured the number concentration of aerosol particles with diameters larger than 12 nm. The POPS provided the PNSD between 0.15 and 2.9 µm diameter and the integrated total number concentration $(N_{>150})$. The number concentration of particles between 12 and 150 nm (N_{12-150}) was derived from the difference in number concentrations measured with the CPC and the POPS. Both instruments were calibrated before and after the field measurements as described in Pilz et al. (2022a).

The CPC and the POPS were installed downstream of a vertical funnel inlet and a silica dryer in a heated compartment. The relative humidity of the aerosol sample at the instrument's inlet was, on average, 17% and never exceeded 30%. The upper cutoff size (50% sampling efficiency) of the interstitial inlet depends on the ambient wind speed (Pilz et al., 2022a). The median wind speeds of 5.8 m s⁻¹ during the balloon measurements resulted in a median cutoff at 1.4 μm . The PNSD of the POPS was likely affected by the hygroscopic growth of dry particles to wet sizes above the inlet's upper cutoff at high ambient relative humidity. This is particularly relevant for highly hygroscopic particle species like inorganic sea salt in sizes above 0.56 µm concerning a hygroscopic growth factor up to 2.4 at 90% (Zieger et al., 2017). However, this effect is negligible for $N_{>150}$ considering the 2–3 orders of magnitude lower number concentrations of these particles compared to the smaller sizes at around 150 nm.

The processed data (Pilz et al., 2022b) include corrections to standard temperature (273.15 K) and pressure (1,013.25 hPa). A 10-s-centered moving average was applied during data analysis. The N_{12} by the CPC onboard CAMP showed 98% ($R^2 = 0.99$, P < 2.2e-16) counting against a reference CPC (N_{10}) onboard *Polarstern* with a standard deviation of $\pm 20\%$ at 1-Hz sampling. The mean $N_{>150}$ from the POPS was within $\pm 20\%$ of the integrated

PNSD between 150 and 500 nm measured by a mobility particle size spectrometer at 5 min averaging, while the PNSD showed qualitatively good agreement considering the different measurement principles. More details on the intercomparison during MOSAiC can be found in Pilz et al. (2023).

2.3. Balloon-borne meteorological measurements

A custom-built extended meteorological package was deployed on BELUGA on each aerosol profile (Pilz et al., 2023). A cylindrical housing with a wind vane at the rear end contained a standard radiosonde for the measurement of atmospheric pressure, temperature, and relative humidity. A Pitot-static tube at the probe's front and an internal digital compass provided wind speed and direction measurements, respectively (Pilz et al., 2022c). Unfortunately, wind speed measurements were often negatively affected by clogging of the Pitot-static tube from droplets inside clouds. Missing data from the extended meteorology data were substituted by concurrent balloon-borne measurements from an ultrasonic anemometer package (Egerer et al., 2021b) and a radiation package (Lonardi et al., 2022b).

2.4. Cloud boundary analysis

The cloud base and top for each profile observation were determined with the relative humidity measurements by the extended meteorology package complemented by ship-based cloud remote sensing onboard RV Polarstern. The cloud base height was derived from a ceilometer with a 10-m vertical resolution as part of the U.S. Department of Energy Atmospheric Radiation Measurement (ARM) program (Morris and Ermold, 2022). The cloud top was derived from the vertically pointing Ka-band ARM Zenith cloud radar reflectivity at 30-m resolution as part of the Cloudnet retrieval (Engelmann et al., 2023). In the case of scattered clouds, only the lowest and highest cloud boundaries were considered. For some aerosol profiles, concurrent in situ radiation observations on BELUGA were also available to determine the cloud boundaries (Lonardi et al., 2022b). In the following descriptions, the term cloud can also refer to low-level fog.

2.5. Back trajectory analysis

The air mass history and origin were analyzed with 5-day back trajectories computed with the Lagrangian analysis tool LAGRANTO (Sprenger and Wernli, 2015) based on ERA5 reanalysis data. An ensemble of about 150 trajectories was calculated for each aerosol measurement flight with BELUGA, separated in 10-hPa steps from 1,000 up to 880 hPa (Figure S2). The surface conditions along the trajectories were evaluated based on the ERA5 sea ice concentrations. Three regions were defined: ice-free (IF) for sea ice concentrations from 0% to 15%, the marginal ice zone (MIZ) from 15% to 80%, and finally pack ice (PI) areas from 80% to 100%.

2.6. Lower tropospheric structure analysis

The base height of the lowest temperature inversion (z_i) above the surface was determined for each aerosol profile observation based on the parallel meteorological

observations on the balloon. z_i was determined from the temperature profiles with a custom algorithm based on criteria given by Tjernström and Graversen (2009). An elevated inversion was defined as an atmospheric layer with a positive temperature gradient and a minimum thickness of 20 m. Due to the high vertical resolution of the BELUGA measurements, the temperature profiles resolved small-scale fluctuations in the entrainment zone below the actual inversion. An additional threshold of a minimum temperature increase of 0.5° C across a detected inversion was applied to exclude these layers as inversion bases. In the case of a surface-based inversion, z_i was defined at the inversion top following Brooks et al. (2017).

The cloud-surface coupling states were defined by relating the determined z_i and cloud boundaries for each profile observation. When an elevated inversion was present and z_i was below the cloud base, it was defined as a decoupled cloud case. In turn, when z_i was above the cloud base (usually near the cloud top), it was categorized as a coupled cloud case. In the presence of a surface-based temperature inversion, it was defined as a statically stable case.

3. Overview of observed vertical aerosol distributions

3.1. Lower tropospheric conditions during the BELUGA measurements

Five different synoptic situations described in detail by Lonardi et al. (2022a) affected the tropospheric conditions during the aerosol observations with BELUGA. The temporal evolution of the resulting temperature and moisture profiles was derived from 6-hourly radiosondes (Maturilli et al., 2022) (**Figure 1**). Warmer and moister air masses were frequently observed above colder and dryer surface layers with temperatures below the melting point. Occasionally, warmer and moister air bands were nestled between colder layers. When clouds were present, the

surface layers were usually neutrally stratified. In contrast, surface-based inversions caused stable stratification during rare cloud-free periods. The air temperature (T) for the altitude range of the BELUGA measurements (below 1.25 km) was on average 3°C ranging from -4.4°C on July 2 to 14°C in an exceptionally warm air mass on July 26, 2020. The tropospheric water vapor mixing ratio (r) was on average 4.4 g kg⁻¹ showing a minimum of 0.9 g kg⁻¹ on June 30 and a maximum of 9.3 g kg⁻¹ related to the warm air on July 26, 2020.

3.2. Classification of observed aerosol profiles

An overview of all N_{12-150} and $N_{>150}$ profiles measured with CAMP attached to BELUGA during MOSAiC is shown in Figure 2. The observed vertical particle distribution resulted from the prevailing lower tropospheric structure and the influence of different particle sources and sinks. Stably stratified atmospheric layers featured distinct aerosol stratification, particularly for $N_{>150}$ in the free troposphere above low-level clouds. In contrast, constant particle number concentration over an altitude range reflected well-mixed layers (usually related to clouds). Large vertical gradients in N_{12-150} and $N_{>150}$ were typically observed at temperature inversions that separated turbulent from statically stable atmospheric layers. The indications of continuously descending particle layers were observed along multiple profiles on July 15, most likely related to large-scale air mass subsidence. Increased particle number concentration occurring solely during an ascent or descent profile suggested horizontal inhomogeneity of aerosol layers and highlighted possible temporal variability. In some cases, layers with increased humidity in the free troposphere near the top of a low-level cloud capped by a temperature inversion coincided with layers of enhanced particle number concentration (July 14 and 15, 2020, Figure S3). Occasionally, the layers of increased N_{12-150} occurred without a corresponding increase in $N_{>150}$, and vice versa. This indicated different sources for

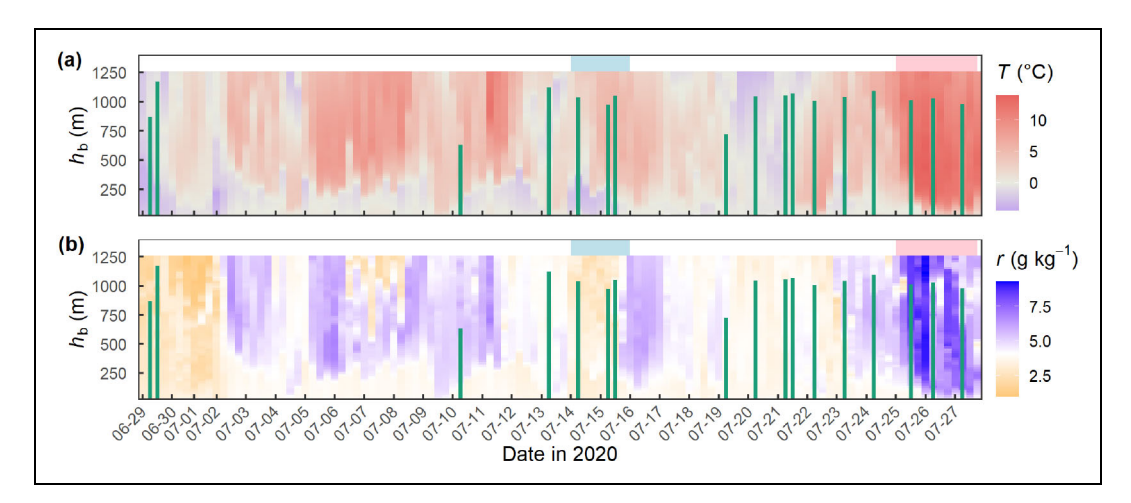


Figure 1. Radiosonde profiles for the time of the BELUGA measurements. (a) Air temperature (T) and (b) water vapor mixing ratio (r) as a function of barometric height (h_b) from 6-hourly radiosondes launched from RV *Polarstern* between June 29 and July 28, 2020, with each green bar representing one BELUGA flight with aerosol measurements. Periods affected by secondary particle formation and long-range transport are shown with blue and pink shaded areas, respectively. BELUGA = balloon-borne modular utility for profiling the lower atmosphere; RV = research vessel.

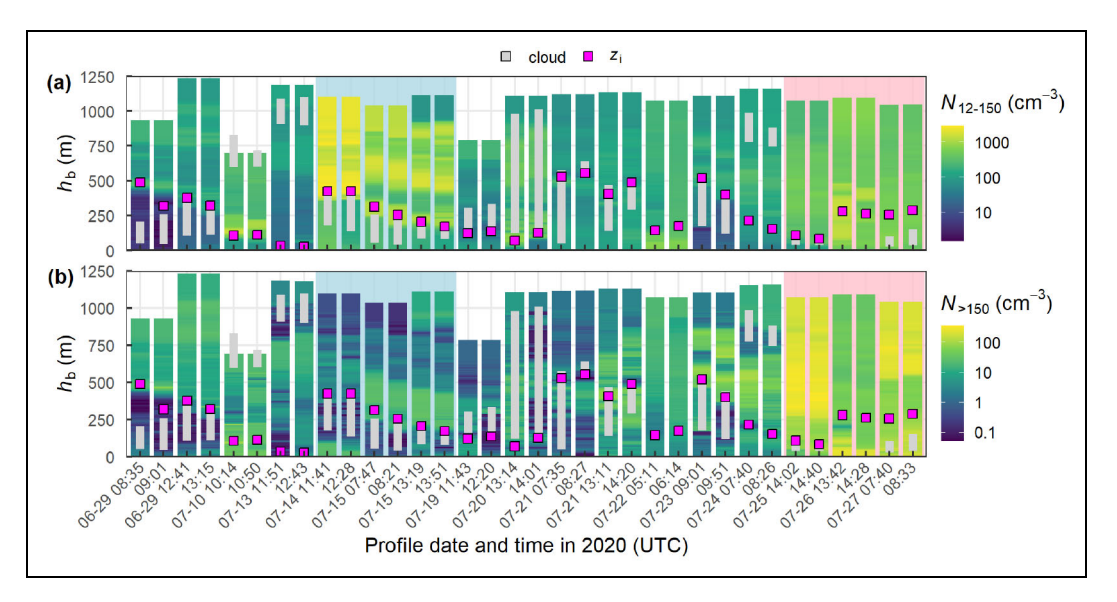


Figure 2. Overview of aerosol profiles. Ascent and descent profiles of particle number concentration (a) in the size range from 12 to 150 nm (N_{12-150}) and (b) above 150 nm ($N_{>150}$) measured with BELUGA. The displayed dates refer to the start of a flight and the times refer to the start of a profile. The magenta squares represent the height of the lowest temperature inversion (z_i) and the gray bars show the cloud cover. Periods affected by secondary particle formation and long-range transport are shown with blue and pink shaded areas, respectively. BELUGA = \underline{b} alloon-borne modular utility for profiling the lower atmosphere.

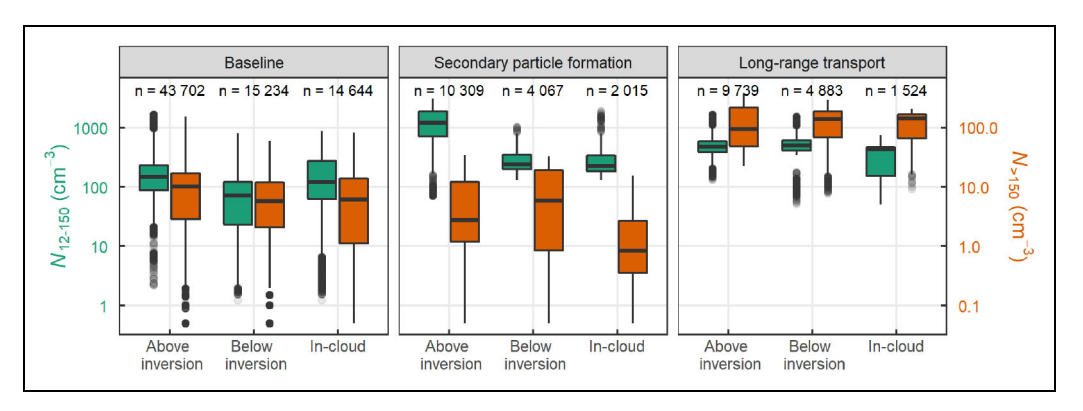


Figure 3. Statistical summary of aerosol profiles. Box–Whisker plot summarizing all profiles of N_{12-150} (green, left *y*-axis) and $N_{>150}$ (orange, right *y*-axis), separated into regions above the lowest inversion, below the lowest inversion, and in-cloud. The observations were grouped into 3 periods: baseline days, secondary particle formation, and long-range transport, as shown in **Figure 2**.

particles of the 2 size ranges. Inside clouds, droplet activation caused a depletion of $N_{>150}$, while N_{12-150} was only partially affected because a fraction of these particles was too small to act as CCN. The reduction of N_{12-150} within clouds compared to the turbulent cloud-mixed layer (CML) extending below the cloud base was usually below 50%.

Three main periods were identified based on the observed values of N_{12-150} and $N_{>150}$ in combination with the back trajectories. The baseline period covered all days except for 2 periods with significantly increased particle number concentrations resulting from different sources (shaded blue and pink areas in **Figure 2**). On July 14 and 15, 2020, highly increased N_{12-150} were possibly the result of secondary particle formation (details in Section 5.1), while long-range transport was identified as the source for extraordinarily high $N_{>150}$ related to the exceptionally

warm and moist air mass between July 25 and 27, 2020 (details in Section 5.3). The 3 periods, baseline, secondary particle formation, and long-range transport, were further separated into regions above z_i below z_i , and in-cloud. Note that the region above z_i does not necessarily represent the free troposphere. In-cloud segments of the profiles were mainly located in the region below z_i on 19 profiles and entirely above z_i on 11 profiles. Cloud-free scenarios were observed during 4 profiles. **Figure 3** and Table S1 summarize the N_{12-150} and $N_{>150}$ profiles for the different periods and atmospheric layers.

The baseline days represented the clean summertime Arctic with low median values of N_{12-150} of 71 cm⁻³ and $N_{>150}$ of 6 cm⁻³ below z_i . These values were well within the range of the continuous observations onboard RV *Polarstern* (Boyer et al., 2023). Above z_i median values

of N_{12-150} and $N_{>150}$ were about 2 times higher than below. CCN activation reduced median in-cloud $N_{>150}$ to a similar level as below z_i , with clouds being mainly located below z_i on 9 profiles and above on 11 profiles. In contrast to $N_{>150}$, median values of N_{12-150} inside clouds were 1.7 times higher than in the below z_i region. Thus, a large share of the observed particles between 12 and 150 nm was often too small to be activated to CCN but could still be washed out when colliding with cloud droplets. Peak values of N_{12-150} and $N_{>150}$ were about 8 times higher than the median below z_i values. The lowest values of N_{12-150} of 15 cm⁻³ were observed on June 29, while $N_{>150}$ were occasionally fully depleted inside clouds from CCN activation.

During the period affected by secondary particle formation on July 14 and 15, 2020, the vertical particle distribution showed highly increased N_{12-150} in the free troposphere above the lowest temperature inversion. The median values of N_{12-150} above z_i were about 8 times higher compared to baseline days. In contrast, $N_{>150}$ was, on average, 3 times lower above z_i than on baseline days. Below z_i about 3 times higher N_{12-150} were likely caused by entrainment, while $N_{>150}$ was similar to baseline days. Inside the clouds that were located below z_i , N_{12-150} was almost the same as for the entire region below z_i , $N_{>150}$

was almost fully depleted by CCN activation inside clouds, thus indicating high supersaturation. The observed peak N_{12-150} values of about 3,000 cm⁻³ above the central Arctic sea ice were so far only measured during new particle formation events (Baccarini et al., 2018; Kecorius et al., 2019).

The days from July 25 to 27, 2020, showed exceptionally high values of $N_{>150}$, particularly at low altitudes. $N_{>150}$ was 25 times higher below z_i , 10 times higher above z_i , and about 30 times higher inside clouds than on baseline days. Such high $N_{>150}$ inside clouds suggest that cloud formation during long-range transport events can result in high droplet number concentrations. The N_{12-150} enhancement was less pronounced, with median values in the range of maximum levels during baseline days. The observed values of $N_{>150}$ were comparable to a pollution event during a warm air intrusion in the springtime Arctic haze period of MOSAiC (Dada et al., 2022).

4. Effects of air mass origin on aerosol vertical distribution

The following section assesses potential linkages between air mass history and vertical aerosol abundance (**Figure 4**). The N_{12-150} and $N_{>150}$ profiles were summarized per BELUGA flight for above z_b below z_b and in-cloud regions.

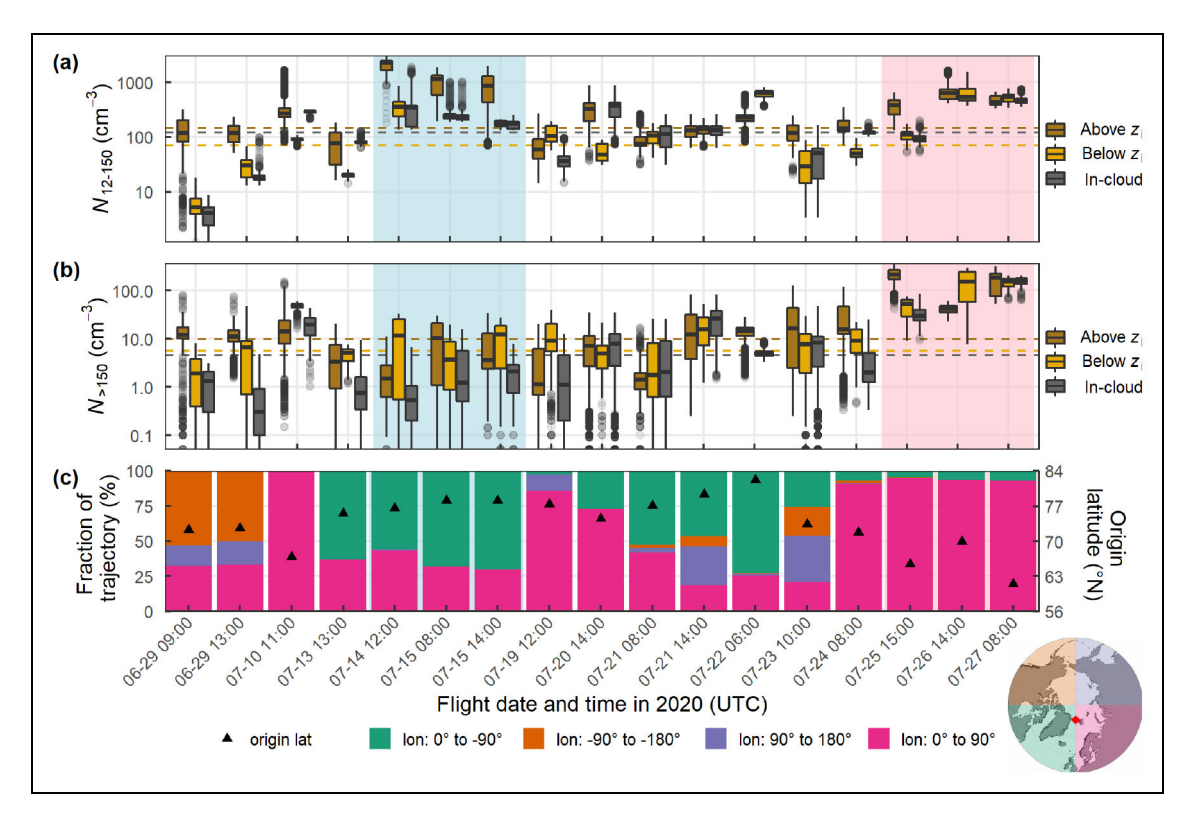


Figure 4. Particle number concentration profiles related to air mass origin. Box–Whisker plots for (a) N_{12-150} and (b) $N_{>150}$ summarized for above z_i , below z_i and in-cloud regions on each BELUGA flight (ascent and descent). The shaded blue and pink areas indicate the periods affected by secondary particle formation and long-range transport, respectively. The dashed lines represent the median N_{12-150} and $N_{>150}$ of all profiles during baseline days. (c) The fraction of time air masses spent in different origin sectors before arriving at RV *Polarstern*, with the median origin latitude of each 5-day back trajectory ensemble shown as black triangles. The origin sectors are illustrated on the map on the bottom right with the mean RV *Polarstern* position displayed as a red square. BELUGA = <u>b</u>alloon-borne modular <u>utility</u> for profiling the lower <u>a</u>tmosphere; RV = research vessel.

Enhanced particle number concentrations were identified by relating median values per flight to the median values of the baseline days (dashed lines in Figure 4). The 5-day back trajectory ensembles were analyzed for the fraction of time that the air masses spent in 1 of the 4 origin sectors before arriving at RV Polarstern. The sectors were divided into the longitude domains from 0° to -90° , -90° to -180° , 90° to 180° , and 0° to 90° with latitudinal limits at 50°N and 90°N. This approach is biased by the location of RV Polarstern in the Fram Strait region near the zero meridian, and thus arriving air masses showing the highest share of travel time in the Barents Sea sector (lon: 0° to 90°) and the Greenland sector (lon: 0° to -90°). However, general trends can be derived in combination with the median origin latitude of each trajectory ensemble. We consider the inner Arctic as the region north of the 10°C July isotherm that is roughly located at a latitude of 70°N. All air masses that originated further south are considered as long-range transport. Following this definition, most of the observed air masses were of inner Arctic origin, while long-range transport was observed in 4 cases.

When inner Arctic air masses showed the highest contribution from the Greenland sector (lon: 0° to -90°), they were often related to increased N_{12-150} without significant $N_{>150}$ enhancement. The period related to secondary particle formation on July 14 and 15 showed trajectories mainly traveling above the Greenland Sea. On July 22, 6 times higher median N_{12-150} were observed below z_i in an air mass coming from ice-covered areas north of Greenland about 300 km away from RV *Polarstern*. These particles likely originated from secondary particle formation near the surface on this cloud-free day featuring a stable surface-based inversion.

In 3 inner Arctic air masses, the shallow layers of increased $N_{>150}$ were observed above z_i . This was the case on June 29 in trajectories coming from the Beaufort Sea sector (lon: -90° to -180°), on July 23 within air from the East Siberian Sea sector (lon: 90° to 180°), and on July 24 in air from the Barents Sea sector (lon: 0° to 90°). We hypothesize that these shallow particle layers with increased $N_{>150}$ up to $130~{\rm cm}^{-3}$ represent pollution plumes that were transported from further south outside of the Arctic as indicated by the back trajectories.

More obvious long-range transport with the highest $N_{>150}$ values occurred from the Barents Sea sector (lon: $0^{\circ}-90^{\circ}$), particularly below z_i . Besides the aforementioned pollution event between July 25 and 27, 10 times higher median $N_{>150}$ values below z_i were observed on July 10. The back trajectories for these cases suggest significant low-altitude pollution transport from anthropogenic sources in Eastern Europe. However, due to the limited number of profiles, deeper analysis is necessary to determine the impact of transported pollution plumes on low-level clouds above sea ice in summer.

5. Case studies of aerosol processes 5.1. Secondary particle formation results in increased free tropospheric particle numbers

In this section, we describe the profiles observed during a period when secondary particle formation affected the particle number concentrations observed with BELUGA on July 14, 2020 (**Figure 5**). The potential temperature (θ) profile shows a weakly stable layer below a shallow temperature inversion at 425 m height, followed by a stably stratified free troposphere aloft. The water vapor mixing ratio (r) was low throughout the profile with an average value of 3 g kg⁻¹. An increase in r above z_i indicates

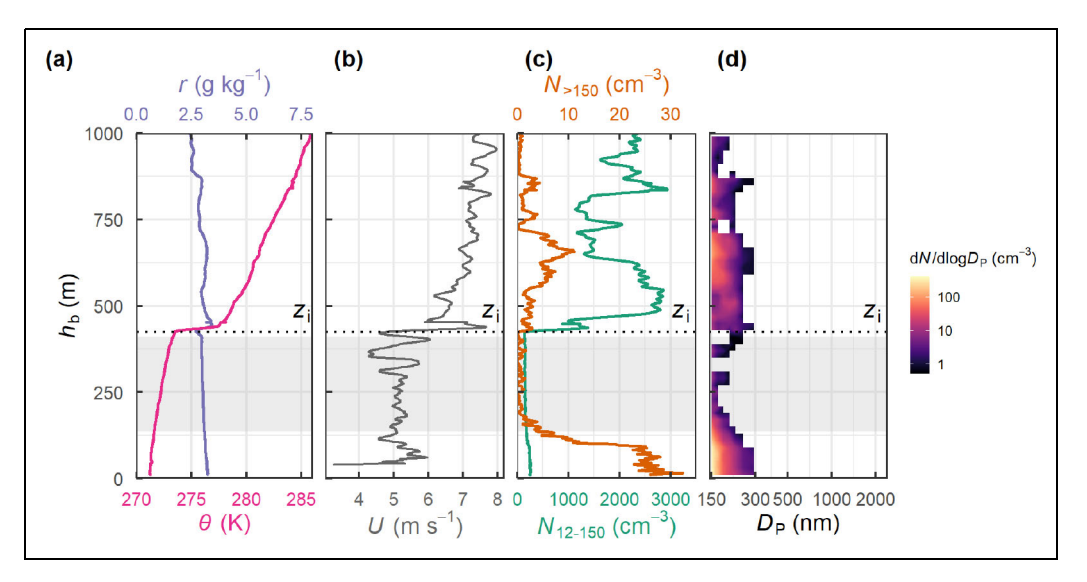


Figure 5. Profile measurements on July 14. Profiles of (a) potential temperature (θ) and water vapor mixing ratio (r), (b) wind speed (U), (c) N_{12-150} and $N_{>150}$, and (d) particle number size distribution (PNSD) of the POPS measured with BELUGA from 12:28 to 13:00 UTC on July 14, 2020. The gray shaded area represents a low-level cloud, and the horizontal dotted line shows z_i . POPS = portable optical particle spectrometer; BELUGA = \underline{b} alloon-born \underline{e} modular utility for profiling the lower atmosphere.

a shallow humidity inversion above the cloud top. The wind speed (U) profile showed a significant decoupling of the above and below inversion layers by median U of 7 and 5.1 m s⁻¹, respectively. Due to the presence of a low-level cloud, coupled with the surface, turbulent mixing occurred below z_i , resulting in approximately constant values of N_{12-150} and $N_{>150}$ below the cloud base. CCN activation inside the cloud caused an almost complete depletion of $N_{>150}$, while N_{12-150} decreased by 35% compared to the values below the cloud base. The maximum values of N_{12-150} of 3,000 cm⁻³ were observed in the free troposphere, in contrast to very low $N_{>150}$ with a maximum of 10 cm⁻³, about one-third of the near-surface values. The PNSD above 150 nm showed only particles below 300 nm below and above the inversion.

The temperature inversion hampered the vertical particle exchange, resulting in a large gradient in N_{12-150} of 38 cm⁻³ m⁻¹ at z_i . However, the median N_{12-150} of 235 cm^{-3} below z_i were 3 times higher compared to baseline days. Hence, a fraction of the particles from the free troposphere was likely entrained into the region below z_i . This assumption is supported by the *U* profile showing a significant peak right above z_i . The static stability inside the temperature inversion enabled a wind speed increase, which, in turn, enhanced friction and turbulence, thus aiding cloud-top entrainment (Solomon et al., 2011; Egerer et al., 2021a). The observed high numbers of N_{12-150} (median of 2,280 cm⁻³) in combination with low $N_{>150}$ (median of 1.75 cm⁻³) above z_i suggest secondary particle formation as a source. The absence of larger particles might have resulted in a low condensation sink for precursor vapors, a precondition for secondary particle formation (Kulmala et al., 2004). However, without size information on the particles between 12 and 150 nm, we can only hypothesize about the possible sources and processes leading to the formation and likely growth of these free tropospheric particles. During the summer melt season, biogenic precursors are the main drivers of new particle formation in the Arctic (Beck et al., 2021; Schmale and Baccarini, 2021). The 5-day back trajectories from the heights above the inversion showed an inner-Arctic air mass (above 76°N) with influences from the Barents Sea, Svalbard, and the Greenland Sea (Figure S2). These regions south of the ice edge are biologically active, with the upper ocean layer as a potential source of reactive vapors involved in secondary particle formation, such as dimethyl sulfide (DMS) or oxygenated volatile organic compounds (Mungall et al., 2017; Wohl et al., 2023). Ammonia emissions from seabird colonies at the coastline of Svalbard can also enhance particle growth (Willis et al., 2016; Beck et al., 2021). DMS can have a lifetime of 5-20 days in this region (Ghahreman et al., 2019) and oxidizes into the aerosol precursors sulfuric acid and methanesulfonic acid (Boyer et al., 2024). A selective analysis of the trajectories arriving above the inversion showed that the air mass had last been at surface levels about 90 h prior to arrival at RV Polarstern, had last traveled over IF regions 60 h before arrival, and slowly descended during the past 44 h (Figure S4). The descent of the air masses is further indicated by lowering particle layers in the aerosol profiles on July 15

(Figure S5). In addition, the observed humidity inversions on July 14 and 15 (Figure S3) are often the result of moisture advection from beyond the ice edge (Brooks et al., 2017; Egerer et al., 2021a). This air mass history suggests 2 possible scenarios. First, the secondary particle formation occurred close to the open ocean surface after the chemical processing of DMS, and the nucleated particles grew during transport in an environment with condensable vapors that supported growth without reducing particle numbers. Second, the gaseous DMS was lifted with the air mass, was chemically processed during transport, and the secondary particle formation occurred at higher altitudes. An increase in solar radiation above low-level clouds might have supported photochemical reactions of the precursor vapors in the latter scenario (Wehner et al., 2015). In any case, the source for the precursor vapors was likely south of the ice edge, and the high numbers of N_{12-150} highlight the importance of free tropospheric particles for the boundary layer above sea ice, as previously found in a modeling study by Price et al. (2023). Additional airborne measurements of the PNSD down to nucleation mode sizes in combination with precursor vapors are necessary to further investigate potential processes.

5.2. Particle advection by a low-level jet below a decoupled cloud

A layer of enhanced particle number concentration related to a low-level jet (LLJ) was observed below a decoupled cloud on July 24, 2020 (Figure 6). During the balloon ascent, the θ profile depicts a statically stable layer extending from the surface to 650 m, where the decoupled CML begins. The lower part of the stable layer that interacted with the sea ice showed a lower slope in θ and r up to z_i at 215 m height. The CML was neutrally stratified with a higher r of 5.4 g kg⁻¹ compared to the layer below z_i . A warmer and dryer air mass was located above the cloudcapping main inversion at 955 m height. The U profile showed a gradual increase up to a maximum of 8.6 m s⁻¹ at about 554 m height with intermittent minima at 150 and 370 m height. This U profile shows an LLJ with a core between 370 and 650 m height. Inside the CML above the LLJ, the *U* profile showed significant variations around the mean value of about 6.7 m s⁻¹, indicating turbulence and vertical mixing.

The aerosol profiles followed an increasing trend with height similar to the U profile. A pronounced layer of N_{12-150} and $N_{>150}$ values was located in the upper part of the LLJ between 550 and 650 m. A distinct negative gradient in particle number concentrations coincided with the upper end of the LLJ core and the lower end of the CML at 650 m. Inside the CML, N_{12-150} and $N_{>150}$ were almost constant below the cloud base. CCN activation inside the cloud caused a complete depletion of $N_{>150}$ and a reduction in N_{12-150} of about 35% compared to levels below the cloud base. The PNSD did not show many size variations along the profile, with particles mainly below 400 nm. The few remaining particles not activated inside the cloud were below 220 nm. The particle layer between 550 and 650 m was presumably advected by the

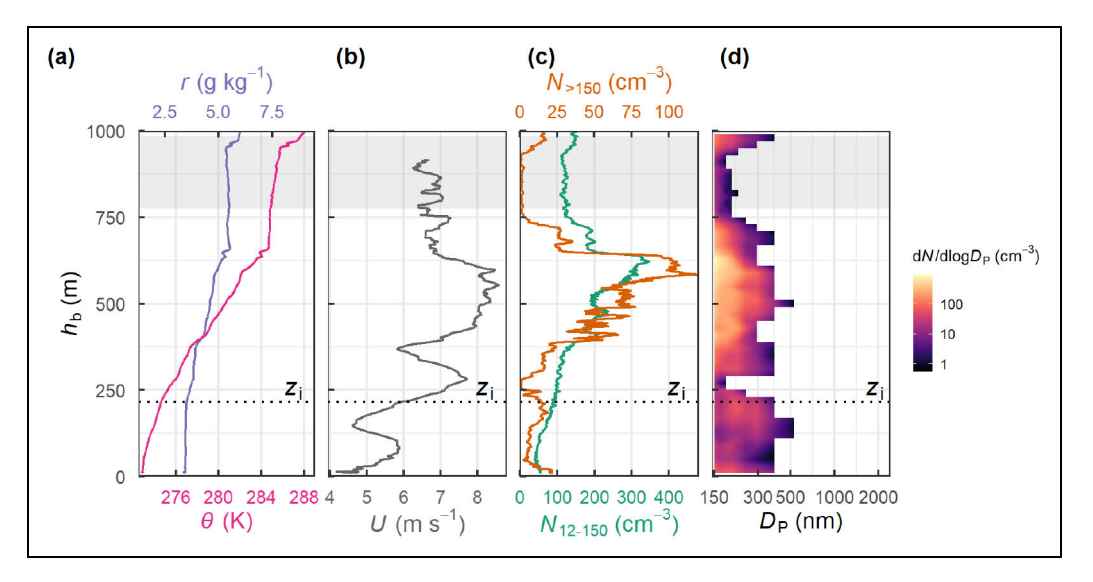


Figure 6. Profile measurements on July 24. The same as in **Figure 5** for an ascent profile from 07:40 to 08:26 UTC on July 24, 2020.

LLJ. Shear forces at the lower edges of the LLJ core induced turbulent mixing that resulted in variations in $N_{>150}$ and N_{12-150} , visible due to the static stability. In the same way, particles were likely mixed upward into the CML at the upper edge of the LLJ. However, within the CML, continuous turbulence dispersed the particles, resulting in fewer observable variations in $N_{>150}$ and N_{12-150} . A detailed study on the effects of LLJs in the stable Arctic atmosphere is shown in recent work by Egerer et al. (2023). In conclusion, the LLJ facilitated enhanced horizontal transport and vertical mixing of particles, thus providing CCN for the decoupled cloud layer from below. Given the high $N_{>150}$ above 100 cm⁻³, the source of the particles was most likely anthropogenic. As indicated by the back trajectories, the air mass was transported from Eastern Europe and the Kola peninsula before arriving at RV Polarstern (Figure S2).

5.3. Long-range transported pollution supports fog

On July 27, 2020, high $N_{>150}$ related to long-range pollution transport supported the formation of a dense fog layer inside a surface-based inversion. The fog layer at altitudes below the detection limit of the cloud radar was observed by radiation measurements conducted in parallel to the aerosol measurements using BELUGA. The warm air with temperatures up to 12.3°C caused the formation of a strongly stable inversion of 0.056 K m⁻¹ during advection over sea ice fixed at the melting point (**Figure 7**). The r profile showed an increase from 3.5 g kg $^{-1}$ at the surface to 6 g kg⁻¹ at the top of the fog layer at about 100 m height. Aloft, r decreased up to a height of about 580 m, where a layer of enhanced moisture existed up to 920 m. The *U* profile showed the lowest values of 3.3 m s⁻¹ inside the fog layer, a gradual increase up to a maximum of 7.8 m s^{-1} at 615 m, and a slightly decreasing trend aloft.

The N_{12-150} and $N_{>150}$ profiles showed opposing vertical trends from the surface to the top of the fog layer (R^2 = 0.74, P < 2.2e-16). Inside the fog, $N_{>150}$ gradually decreased from the bottom to the top due to an increasing CCN activation inside the statically stable layer. This indicates a higher supersaturation at the top of the fog layer, likely caused by radiative cooling. Strong positive gradients in N_{12-150} and $N_{>150}$ at the top of the fog layer suggest that the particles of both size ranges were activated to cloud droplets inside the fog layer below. Aloft, N_{12-150} and $N_{>150}$ uniformly decreased toward the top of the inversion and remained rather constant up to 580 m height. Inside the moister layer above, $N_{>150}$ increased up to 313 cm⁻³, whereas N_{12-150} gradually decreased to values similar to the surface concentration. The PNSD showed significantly larger particles than during the other cases with sizes up to 1 µm, particularly in the layer above 580 m. Inside the fog layer, the PNSD indicates a decreasing CCN activation diameter with height.

The profiles on July 27 were observed during a period of significantly enhanced content of absorbing particles measured onboard RV Polarstern between July 26 and 29 (Figure S6). A derived equivalent black carbon mass concentration up to 100 ng m⁻³ on July 26 clearly indicates long-range pollution transport as the particle source. This complies with the back trajectories from July 25 to 27, all coming from continental Eastern Europe (Figure S2). The trajectories from July 24 originated in the same region but further north, indicating that the advection of the pollution plume might have begun with the LLJ, as discussed above. Afterward, the plume potentially increased in number concentration and vertical extent until it reached the sea ice surface on July 26. The plume probably also contained larger sea salt particles, as indicated by the PNSD. They were likely generated during transport above the open ocean considering an average wind speed of 7 m s⁻¹ during the past 120 h estimated by

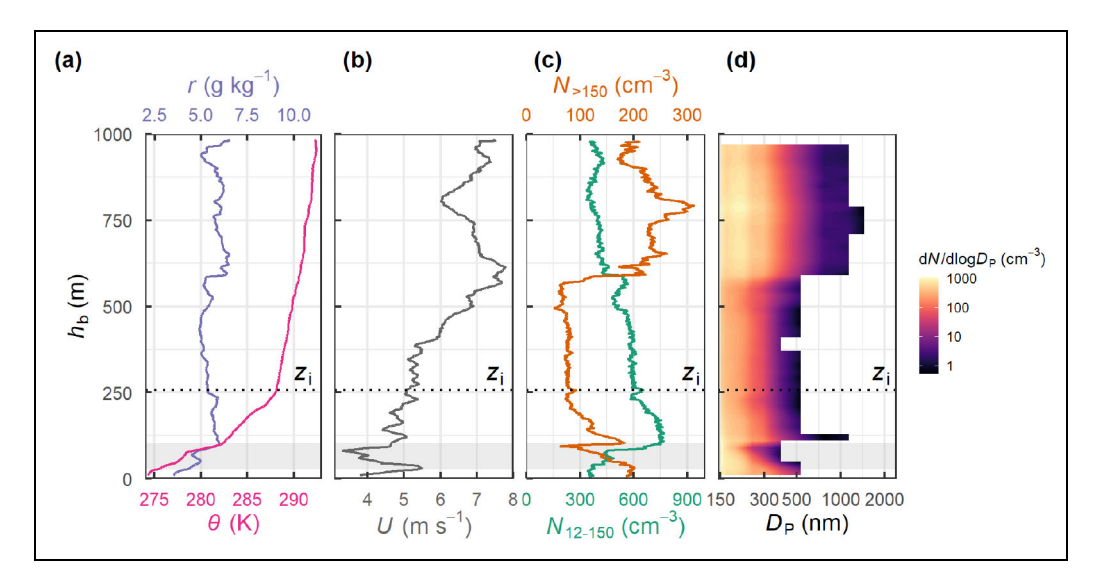


Figure 7. Profile measurements on July 27. The same as in **Figure 5** for an ascent profile from 07:40 to 08:33 UTC on July 27, 2020.

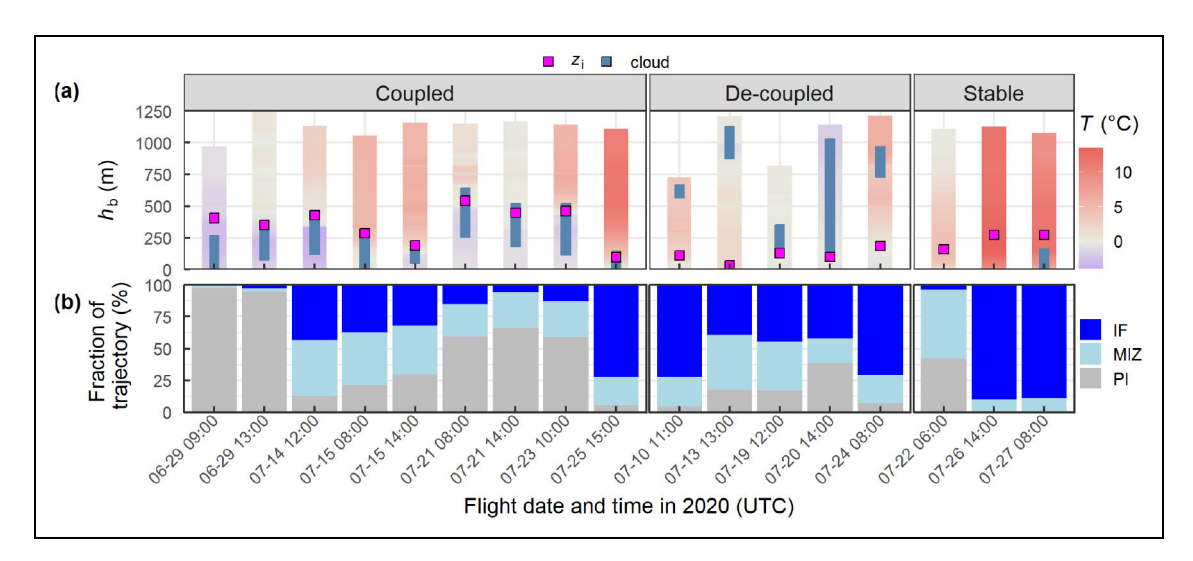


Figure 8. Lower tropospheric structure and surface conditions during air mass history. (a) The thermal structure of the lower troposphere during the aerosol flights (ascent and descent) categorized into 3 commonly observed cases: coupled clouds, decoupled clouds, and stable cases with surface-based inversions. The magenta squares represent z_i , and the blue bars show the cloud cover. (b) The average fraction of time that the air mass spent over ice-free areas (IF), the marginal ice zone (MIZ), and the pack ice (PI) during the past 5 days before arriving at RV *Polarstern* at the time of the aerosol flight. RV = research vessel.

the distance of the average trajectory origin location 2,940 km away from RV *Polarstern*.

The vertical transport of the air mass arriving on 27 showed that the pollution plume was mainly advected at low altitudes with a low mean cloud cover of 6.2% over the past 5 days of travel (Figure S7). This case provides evidence that long-range pollution transport to the central Arctic at low altitudes can occur in summer without efficient wet scavenging by low-level clouds above the open ocean. Moreover, the transported $N_{>150}$ provided many CCN that enabled the formation of a low-level fog layer with a high droplet number concentration likely above 100 cm^{-3} . The dense fog resulted in a low average visibility of 232 m during the balloon profile (Figure S8) with an

estimated optical thickness of 1.68 with a vertical extent of 100 m (Bäumer et al., 2008). Such an optically thick and warm fog inside a moist surface-based inversion can significantly enhance the net downward heat flux, thereby possibly increasing sea ice melt (Tjernström et al., 2019).

6. Effects of lower tropospheric structure on aerosol vertical distribution

6.1. Lower tropospheric structures related to air mass history

Three typical lower tropospheric structures were observed during the aerosol profile measurements: coupled clouds, decoupled clouds, and statically stable cases (**Figure 8a**). Coupled, decoupled, and stable cases were observed on

18, 10, and 6 profile observations, respectively. Cloud-free conditions were observed during 4 stable cases (July 22 and 26), while 2 stable cases on July 27 showed low-level fog (see Section 5.3). Concerning that the lower tropospheric structure alters with the time that an air mass interacts with sea ice after advection (Tjernström et al., 2019), we attempt to relate them to the air mass history. The 5-day back trajectories were analyzed in terms of the average fraction of time each trajectory ensemble per balloon flight spent above ice-free (IF) areas, the marginal ice zone (MIZ), and the pack ice (PI) (**Figure 8b**). Note that RV *Polarstern* drifted mainly in PI areas for the time of the balloon measurements before entering the MIZ for July 26 and 27.

In coupled cases, the clouds induced deeper turbulent mixing resulting in elevated values of z_i at an average of 350 m, compared to the decoupled cases with shallow surface layers with a mean value of z_i of 110 m. The atmosphere below z_i was colder during cloud coupling than in the decoupled cases at an average T of -1.2° C and 0.3° C, respectively. Similarly, the surface-coupled clouds below z_i were colder compared to the decoupled clouds. This result aligns with the findings by Shupe et al. (2013), who concluded that cloud-surface coupling is more likely to occur when the cloud layer is cold enough to enable mixing with the cold surface layer. In two of the decoupled cases (July 19 and 20), the cloud base was close to z_i in contrast to the other cases of this category. The potential temperature profiles of the 2 cases showed a stable stratification with gradients of 0.012 and 0.008 K m⁻¹ inside the clouds on July 19 and 20, respectively (Figure S9), thus suggesting insufficient cloud-driven turbulence to connect the cloud with the turbulent surface layer (Brooks et al., 2017). A recent study by Lonardi et al. (2023) suggests that turbulence driven by cloud-top radiative cooling in low-level Arctic clouds could be reduced by a second cloud layer aloft. This is consistent with the Cloudnet observations showing a second cloud layer at about 2 km on July 19 and a rather broken cloud with a main upper and lower layer on July 20.

In the presence of clouds, the back trajectory analysis indicated that the longer an air mass traveled over sea ice, the more likely it would be observed to be coupled to the surface. For coupled cases, the mean time air masses spent over sea ice (MIZ and PI) was 92 h. With an average time of 55 h over ice, decoupled cloud cases seemed to occur in rather early stages after air masses were advected over sea ice. However, the few observed cases can only provide a suggestion rather than support broader statistics.

The stable cases with a surface-based temperature inversion are mainly the result of warm air advection over the sea ice. However, different temperature profiles resulted from the time that the air masses spent over ice (see Section 6.4). Lower temperatures were observed on July 22 after the air mass cooled down during 115 h of travel over ice. This contrasted with the air mass that was recently advected over ice (12 h) on July 26 and 27.

Interestingly, the absence of clouds on July 22 and 26 probably did not result from a lack of moisture and/or aerosol particles as found by Loewe et al. (2017). The observed average $r=3.9~{\rm g~kg^{-1}}$ and $N_{>150}=12~{\rm cm^{-3}}$

on July 22 were well in the range of other profiles with cloud cover and well above that on July 26 with 5.2 g kg⁻¹ and 85 cm⁻³, respectively. In particular, the general conditions and profiles were very similar on July 26 and 27, but low-level fog was only formed on July 27. Perhaps the air did not cool down sufficiently on July 26 to cause condensation, or the fog had already formed before the air mass advected into the MIZ on July 27 but not on July 26.

6.2. Aerosol profiles in coupled cloud cases

The values of N_{12-150} and $N_{>150}$ in coupled cloud cases covered several orders of magnitude. The normalization of the particle number concentration profiles with the median number concentration below the cloud of each individual profile was applied to provide a useful overview of all profiles in this category. The region below the cloud is not affected by CCN activation and is represented by surface-based observations in these coupled cases, thus enabling a rough estimation of particle concentration aloft from the surface measurements. The height axis was rescaled by z_i .

The median profiles of all coupled cloud cases show a neutral to weakly stable thermodynamic stratification below z_i ($b_b/z_i < 1$) dominated by low-level clouds (**Figure 9**). Cloud-driven turbulence caused the mixing of moisture and aerosol particles, which is represented by constant r and N_{12-150} profiles. CCN activation inside clouds caused, on average, a decrease in $N_{>150}$ of 65% compared to below cloud levels, while the reduction in N_{12-150} was 15%. In the stably stratified free troposphere

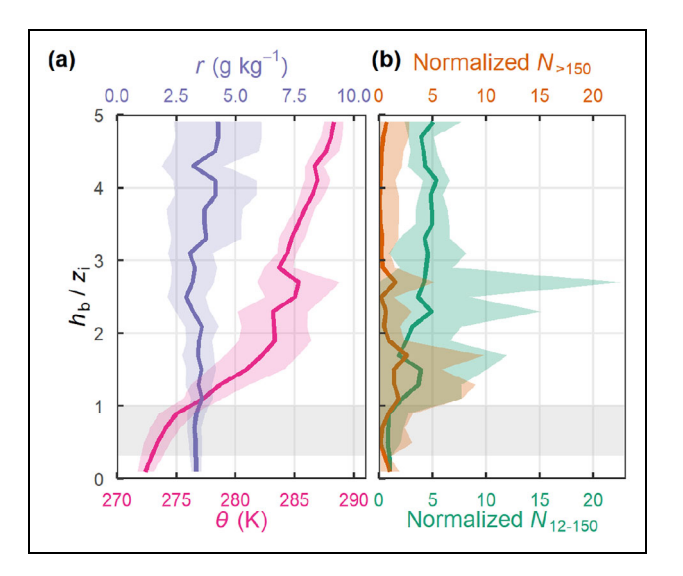


Figure 9. Median profiles for coupled cloud cases. Median profiles of (a) θ and r and (b) normalized N_{12-150} and $N_{>150}$ of all coupled cloud cases (18 profiles, n=42,491 for N_{12-150} and $N_{>150}$). The shaded areas represent the associated single standard deviation. The vertical axis was normalized by z_i , and particle concentrations were normalized by the median below cloud concentration of each profile. The gray-shaded areas represent the median normalized cloud cover.

above z_i ($h_b/z_i > 1$), θ and r increased with height. A steady increase in N_{12-150} with height of up to 5 times higher N_{12-150} levels compared to the below cloud region implies a free tropospheric source for these particles. In contrast, the enhanced values of $N_{>150}$ were observed in shallow layers right above the inversion at the cloud top. The layers of increased $N_{>150}$ either originate from longrange transport or evaporated cloud particles that were detrained from the cloud. Increasing r, N_{12-150} , and $N_{>150}$ in the cloud-top region starting below the inversion top indicate moisture and particle entrainment from aloft, thus potentially sustaining the lifetime of Arctic low-level clouds above the sea ice (Solomon et al., 2011; Morrison et al., 2012; Shupe et al., 2013; Igel et al., 2017; Egerer et al., 2021a; Williams and Igel, 2021).

6.3. Aerosol profiles in decoupled cloud cases

Similar to the coupled cloud cases in the previous section, N_{12-150} and $N_{>150}$ were normalized by the median particle number concentration below z_i of each profile for all decoupled cloud cases. The median profiles show a neutrally stratified region below the lowest inversion, and constant r and N_{12-150} profiles suggest a well-mixed layer just above the surface (Figure 10). However, a negative $N_{>150}$ gradient with increasing height indicates a nearsurface particle source that is not dispersed in the entire height range below z_i . In decoupled cloud cases, the windshear-driven turbulence induced at the surface often decreases with height until it reaches a nonturbulent state between 50- and 100-m altitude (Brooks et al., 2017). Thus, the turbulent mixing of particles emitted near the surface might not be efficient enough up to z_i . In this case, the N_{12-150} profiles should show similar trends, which

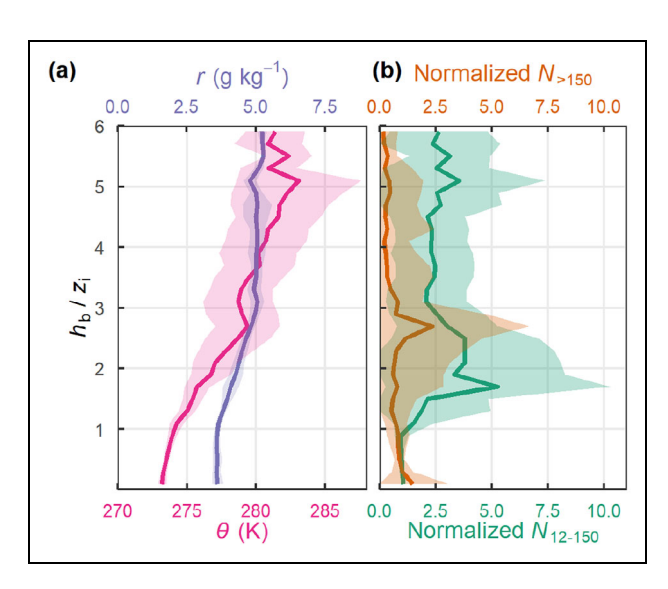


Figure 10. Median profiles for decoupled cloud cases.

Median profiles of (a) θ and r and (b) normalized N_{12-150} and $N_{>150}$ of all decoupled cloud cases (10 profiles, n=26,143 for N_{12-150} and $N_{>150}$). The shaded areas represent the associated single standard deviation. The vertical axis was normalized by z_i and particle concentrations were normalized by the median below z_i concentration of each profile.

were only observed on a few occasions but less pronounced than for the larger particles. This suggests that the particle source near the surface emitted rather large particles. At the observed generally low values of $N_{>150}$ below z_i , only a few naturally emitted particles from open leads (Held et al., 2011) or even local contamination by installations on the ice are possible sources. However, the long-term observations onboard RV *Polarstern* are more appropriate to determine surface sources considering the relatively low sampling time of the balloon profiles near the surface facing low number concentrations. Still, the results highlight the height dependence of particle concentration in the lowest hundred meters above sea ice, particularly in less turbulent conditions.

The mainly stably stratified region above z_i shows a larger moisture content, likely related to the presence of clouds. Because of the high variability in cloud cover across the observed profiles, no average cloud location is displayed in **Figure 10**. Hence, the median aerosol profiles above z_i were affected by CCN activation and might not be fully representative of this atmospheric layer. However, the general tendency of an N_{12-150} increase with height and occasionally observed layers of increased $N_{>150}$ above z_i allow us to conclude that surface-based observations are not representative of decoupled cloud layers. In addition, particularly for the smaller particles, it appears that the source is remote and not at the surface since the concentrations aloft are multiple times higher.

6.4. Aerosol profiles in statically stable cases

The stable cases with a surface-based inversion are displayed in **Figure 11**. Again, we have normalized the values of N_{12-150} and $N_{>150}$ by the median aerosol particle number concentration below z_i of each profile. Median

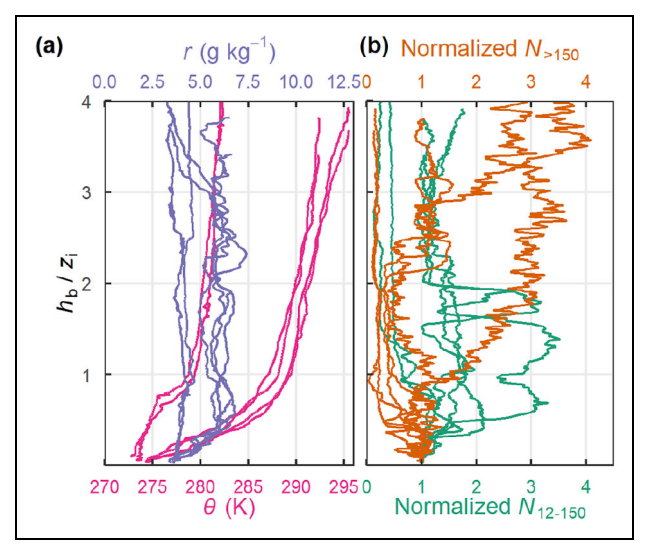


Figure 11. Normalized profiles for stable cases. (a) Profiles of θ and r and (b) normalized N_{12-150} and $N_{>150}$ profiles of all stable cases (6 profiles, n=19,300 for N_{12-150} and $N_{>150}$). The vertical axis was normalized by z_i , and particle concentrations were normalized by the median below z_i concentration of each profile.

profiles were not provided due to the low number of 6 cases. The θ and r profiles reflect the significant difference between the inner Arctic air mass on July 22 (2 profiles on the left) and the long-range transported warm air masses on July 26 and 27 (4 profiles on the right). θ and r were higher, and the surface-based inversion was much more stable during the long-range transport event. The normalized N_{12-150} and $N_{>150}$ profiles showed a high variability above a shallow mixed layer close to the surface. Thus, turbulent mixing in stable cases was limited to the lowest meters above the surface, and distinct aerosol layering occurred throughout the stably stratified lower troposphere. Such shallow surface layers would allow the accumulation of precursor vapors emitted from the surface in the presence of a low condensation sink, thus potentially fostering secondary particle formation. In conclusion, in statically stable cases, surface-based measurements are typically not representative of the troposphere aloft and might be biased by the differences in inlet heights, for instance, between the sea ice level and on the ship deck.

7. Summary and conclusions

This study reported tethered balloon-borne aerosol measurements made above the central Arctic sea ice during the MOSAiC expedition in the summer of 2020. Thirty-four profiles of particle number concentration between 12 and 150 nm (N_{12-150}) and above 150 nm ($N_{>150}$) through frequently occurring low-level clouds were analyzed in combination with balloon-borne meteorological measurements, surface-based cloud remote sensing, and 5-day back trajectories.

Enhanced N_{12-150} and $N_{>150}$ were observed above the lowest temperature inversion (z_i) on the majority of profiles, with the average being 2 times higher than below. Inside clouds, CCN activation led to a significant reduction in $N_{>150}$, while the decrease in N_{12-150} was usually below 50%. Hence, the majority of the observed N_{12-150} inside cloud layers were too small to act as CCN, probably smaller than 50 nm (Leaitch et al., 2016; Baccarini et al., 2018; Kecorius et al., 2019; Karlsson et al., 2021, 2022). During a period affected by secondary particle formation, average N_{12-150} values above z_i were 8 times higher compared to baseline days, with maximum N_{12-150} up to 3,000 cm⁻³ in the free troposphere. A pollution plume transported at low altitudes from Eastern Europe showed median $N_{>150}$ that was 25 times higher than on baseline days, with peak $N_{>150}$ up to 310 cm⁻³.

When low-level clouds were coupled with the surface, N_{12-150} in the free troposphere were 5 times higher than below the lowest inversions that were on average at 350 m height. These particles probably originated from secondary particle formation and are potentially entrained at the cloud top (Igel et al., 2017). Once entrained, larger particles can directly act as CCN. Smaller ones may undergo condensational growth into CCN size or collide with cloud particles. Eventually, grown particles are released from droplet evaporation. Concurrent particle entrainment and cloud processing can result in the consistently observed bimodal PNSD above the sea-ice-

covered central Arctic in summer (Heintzenberg and Leck, 2012; Boyer et al., 2023).

In cases where the cloud was decoupled from the surface, enhanced N_{12-150} and $N_{>150}$ were observed above shallow surface layers with mean z_i of 110 m. These particles originated from remote sources beyond the sea ice edge and were horizontally transported within the CML or in statically stable layers below, not captured by surface-based observations. The vertically discontinuous turbulence prevented particles emitted at the surface from being transported up to the decoupled cloud. Therefore, the cloud-surface coupling state should be taken into consideration for aerosol—cloud interaction studies above the Arctic sea ice.

Our study implies a minor role of biogenic precursor vapors emitted from open leads or melt ponds for N_{12-150} above the sea ice. Indications for secondary particle formation near the surface leading to increased N_{12-150} below z_i were only observed on one cloud-free day within an air mass coming from Northern Greenland. The majority of cases with increased N_{12-150} were observed in the free troposphere above surface-coupled clouds. These particles possibly resulted from secondary particle formation based on biogenic precursor vapors advected from south of the ice edge, which is in line with recent findings (Price et al., 2023; Boyer et al., 2024). We hypothesize that the potentially higher solar radiation above clouds could foster the chemical processing of precursors and initiate nucleation at higher altitudes as observed in marine clouds at lower latitudes (Wehner et al., 2015). More vertical measurements covering the PNSD down to the nucleation mode and, ideally, precursor vapors in the Arctic are needed to further investigate potential precursor transport and particle formation processes aloft.

Data accessibility statement

The data sets used in this work were produced as part of the international Multidisciplinary drifting Observatory for the Study of Arctic Climate (MOSAiC) expedition. The tethered balloon-borne data (Egerer et al., 2021b; Lonardi et al., 2022b; Pilz et al., 2022b, 2022c) and the radio-sounding data (Maturilli et al., 2022) are publicly available on PANGAEA (https://www.pangaea.de). The ship-based ceilometer data (Morris and Ermold, 2022) are available via the Department of Energy Atmospheric Radiation Measurement user facility Data Center (https://adc.arm.gov). The Cloudnet remote-sensing data (Engelmann et al., 2023) were generated by the European Research Infrastructure for the observation of Aerosol, Clouds, and Trace Gases (ACTRIS) and are available from the ACTRIS Data Centre (https://cloudnet.fmi.fi/).

Supplemental files

The supplemental files for this article can be found as follows:

Supplemental-Material.pdf.

Acknowledgments

This work was carried out, and data used in this manuscript were produced as part of the international

Multidisciplinary drifting Observatory for the Study of Arctic Climate (MOSAiC) with the tag MOSAiC20192020. We thank all persons involved in the expedition of the research vessel Polarstern during MOSAiC in 2019-2020 (AWI PS122 00) as listed in Nixdorf et al. (2021). Some data were obtained from the Atmospheric Radiation Measurement User Facility, a U.S. Department of Energy Office of Science User Facility Managed by the Biological and Environmental Research Program. We acknowledge ACTRIS and Finnish Meteorological Institute for providing the data set, which is available for download from https:// cloudnet.fmi.fi. Christian Pilz did parts of the analysis for this study during a research stay at the University of Colorado Boulder, supported by Matthew Shupe, John Cassano, Gijs de Boer, Mira Pöhlker, and Birgit Wehner. He is grateful for this opportunity and the fruitful collaboration. We highly appreciate the constructive feedback of the 3 anonymous referees who helped to improve our manuscript.

Funding

We gratefully acknowledge the funding by the Federal Ministry of Education and Research (BMBF), grant/award no. 03F0865A, within MOSAiC 1—"AVANTI: Aerosolvariabilität über dem Nordpolarmeer und dem Meereis" and the Deutsche Forschungsgemeinschaft (DFG, German Research Foundation)—project number 268020496—TRR 172, within the Transregional Collaborative Research Center "ArctiC Amplification: Climate Relevant Atmospheric and SurfaCe Processes, and Feedback Mechanisms (AC)³" in subproject A02. MDS was supported by a Mercator Fellowship as part of (AC)³, the DOE ASR Program (DE-SC0021341), and NOAA cooperative agreement (NA220 AR4320151).

Competing interests

The authors have no competing interests, as defined by *Elementa*, that might be perceived to influence the research presented in this manuscript. MDS is a guest editor for the *Elementa* Special Feature on MOSAiC.

Author contributions

Conducted the tethered balloon-borne measurements during Multidisciplinary drifting Observatory for the Study of Arctic Climate: CP, ML.

Processed the aerosol data, conducted the analysis, and drafted the manuscript: CP.

Computed the back trajectories: BK.

Contributed to the scientific discussion, interpretation of data, revision of the paper, and approved the submitted version of the manuscript: All authors.

References

Abbatt, JPD, Leaitch, WR, Aliabadi, AA, Bertram, AK, Blanchet, JP, Boivin-Rioux, A, Bozem, H, Burkart, J, Chang, RYW, Charette, J, Chaubey, JP, Christensen, RJ, Cirisan, A, Collins, DB, Croft, B, Dionne, J, Evans, GJ, Fletcher, CG, Galí, M, Ghahreman, R, Girard, E, Gong, W, Gosselin, M, Gourdal, M, Hanna, SJ, Hayashida, H, Herber, AB, Hesaraki, S, Hoor, P, Huang, L, Hussherr, R, Irish,

VE, Keita, SA, Kodros, JK, Köllner, F, Kolonjari, F, Kunkel, D, Ladino, LA, Law, K, Levasseur, M, Libois, Q, Liggio, J, Lizotte, M, Macdonald, KM, Mahmood, R, Martin, RV, Mason, RH, Miller, LA, Moravek, A, Mortenson, E, Mungall, EL, Murphy, JG, Namazi, M, Norman, AL, O'Neill, NT, Pierce, JR, Russell, LM, Schneider, J, Schulz, H, Sharma, S, Si, M, Staebler, RM, Steiner, NS, Thomas, JL, von Salzen, K, Wentzell, JJB, Willis, MD, Wentworth, GR, Xu, JW, Yakobi-Hancock, JD. 2019. Overview paper: New insights into aerosol and climate in the Arctic. *Atmospheric Chemistry and Physics* 19(4): 2527–2560. DOI: http://dx.doi.org/10.5194/acp-19-2527-2019.

Baccarini, A, Karlsson, L, Dommen, J, Duplessis, P, Vüllers, J, Brooks, IM, Saiz-Lopez, A, Salter, M, Tjernström, M, Baltensperger, U, Zieger, P, Schmale, J. 2018. Frequent new particle formation over the high Arctic pack ice by enhanced iodine emissions. *Nature Communications* 11: 4924. DOI: http://dx.doi.org/10.1038/s41467-020-18551-0.

Bäumer, D, Vogel, B, Versick, S, Rinke, R, Möhler, O, Schnaiter, M. 2008. Relationship of visibility, aerosol optical thickness and aerosol size distribution in an ageing air mass over South-West Germany. *Atmospheric Environment* **42**(5): 989–998. DOI: http://dx.doi.org/10.1016/j.atmosenv.2007.10.017.

Beck, LJ, Sarnela, N, Junninen, H, Hoppe, CJM, Garmash, O, Bianchi, F, Riva, M, Rose, C, Peräkylä, O, Wimmer, D, Kausiala, O, Jokinen, T, Ahonen, L, Mikkilä, J, Hakala, J, He, XC, Kontkanen, J, Wolf, KKE, Cappelletti, D, Mazzola, M, Traversi, R, Petroselli, C, Viola, AP, Vitale, V, Lange, R, Massling, A, Nøjgaard, JK, Krejci, R, Karlsson, L, Zieger, P, Jang, S, Lee, K, Vakkari, V, Lampilahti, J, Thakur, RC, Leino, K, Kangasluoma, J, Duplissy, EM, Siivola, E, Marbouti, M, Tham, YJ, Saiz-Lopez, A, Petäjä, T, Ehn, M, Worsnop, DR, Skov, H, Kulmala, M, Kerminen, VM, Sipilä, M. 2021. Differing mechanisms of new particle formation at two Arctic sites. Geophysical Research Letters 48(4): e2020G L091334. DOI: http://dx.doi.org/10.1029/2020GL 091334.

Becker, S, Ehrlich, A, Schäfer, M, Wendisch, M. 2023. Airborne observations of the surface cloud radiative effect during different seasons over sea ice and open ocean in the Fram Strait. *Atmospheric Chemistry and Physics* **23**(12): 7015–7031. DOI: http://dx.doi.org/10.5194/acp-23-7015-2023.

Boyer, M, Aliaga, D, Pernov, JB, Angot, H, Quéléver, LLJ, Dada, L, Heutte, B, Dall'Osto, M, Beddows, DCS, Brasseur, Z, Beck, I, Bucci, S, Duetsch, M, Stohl, A, Laurila, T, Asmi, E, Massling, A, Thomas, DC, Nøjgaard, JK, Chan, T, Sharma, S, Tunved, P, Krejci, R, Hansson, HC, Bianchi, F, Lehtipalo, K, Wiedensohler, A, Weinhold, K, Kulmala, M, Petäjä, T, Sipilä, M, Schmale, J, Jokinen, T. 2023. A full year of aerosol size distribution data from the central Arctic under an extreme positive Arctic oscillation: Insights from the Multidisciplinary drifting

- Observatory for the Study of Arctic Climate (MOSAiC) expedition. *Atmospheric Chemistry and Physics* **23**(1): 389–415. DOI: http://dx.doi.org/10. 5194/acp-23-389-2023.
- Boyer, M, Aliaga, D, Quéléver, LLJ, Bucci, S, Angot, H, Dada, L, Heutte, B, Beck, L, Duetsch, M, Stohl, A, Beck, I, Laurila, T, Sarnela, N, Thakur, RC, Miljevic, B, Kulmala, M, Petäjä, T, Sipilä, M, Schmale, J, Jokinen, T. 2024. The annual cycle and sources of relevant aerosol precursor vapors in the central Arctic. *EGUsphere* **2024**: 1–49. DOI: http://dx.doi.org/10.5194/egusphere-2023-2953.
- Brooks, IM, Tjernström, M, Persson, POG, Shupe, MD, Atkinson, RA, Canut, G, Birch, CE, Mauritsen, T, Sedlar, J, Brooks, BJ. 2017. The turbulent structure of the Arctic summer boundary layer during the Arctic summer cloud-ocean study. *Journal of Geophysical Research: Atmospheres* 122(18): 9685–9704. DOI: http://dx.doi.org/10.1002/2017J D027234.
- Burkart, J, Willis, MD, Bozem, H, Thomas, JL, Law, K, Hoor, P, Aliabadi, AA, Köllner, F, Schneider, J, Herber, A, Abbatt, JPD, Leaitch, WR. 2017. Summertime observations of elevated levels of ultrafine particles in the high Arctic marine boundary layer. *Atmospheric Chemistry and Physics* 17(8): 5515–5535. DOI: http://dx.doi.org/10.5194/acp-17-5515-2017.
- Chechin, DG, Lüpkes, C, Hartmann, J, Ehrlich, A, Wendisch, M. 2023. Turbulent structure of the Arctic boundary layer in early summer driven by stability, wind shear and cloud-top radiative cooling: ACLOUD airborne observations. *Atmospheric Chemistry and Physics* **23**(8): 4685–4707. DOI: http://dx.doi.org/10.5194/acp-23-4685-2023.
- Dada, L, Angot, H, Beck, I, Baccarini, A, Quéléver, LL, Boyer, M, Laurila, T, Brasseur, Z, Jozef, G, de Boer, G, Shupe, MD, Henning, S, Bucci, S, Dütsch, M, Stohl, A, Petäjä, T, Daellenbach, KR, Jokinen, T, Schmale, J. 2022. A central Arctic extreme aerosol event triggered by a warm air-mass intrusion. *Nature Communications* 13(1): 1–15. DOI: http://dx.doi.org/10.1038/s41467-022-32872-2.
- Egerer, U, Ehrlich, A, Gottschalk, M, Griesche, H, Neggers, RAJ, Siebert, H, Wendisch, M. 2021a. Case study of a humidity layer above Arctic stratocumulus and potential turbulent coupling with the cloud top. *Atmospheric Chemistry and Physics* **21**(8): 6347–6364. DOI: http://dx.doi.org/10.5194/acp-21-6347-2021.
- Egerer, U, Gottschalk, M, Siebert, H, Ehrlich, A, Wendisch, M. 2019. The new BELUGA setup for collocated turbulence and radiation measurements using a tethered balloon: First applications in the cloudy Arctic boundary layer. *Atmospheric Measurement Techniques* **12**(7): 4019–4038. DOI: http://dx.doi.org/10.5194/AMT-12-4019-2019.
- Egerer, U, Pilz, C, Lonardi, M, Siebert, H, Wendisch, M. 2021b. Tethered balloon-borne measurements of turbulence during MOSAiC leg 4 in July 2020.

- PANGAEA. DOI: http://dx.doi.org/10.1594/PANGAEA.931404.
- Egerer, U, Siebert, H, Hellmuth, O, Sorensen, LL. 2023. The role of a low-level jet for stirring the stable atmospheric surface layer in the Arctic. *EGUsphere* **2023**: 1–23. DOI: http://dx.doi.org/10.5194/egusphere-2023-567.
- Engelmann, R, Althausen, D, Baars, H, Griesche, H, Hofer, J, Radenz, M, Seifert, P. 2023. Custom collection of categorize data from RV polarstern between 29 Jun and 27 Jul 2020. ACTRIS Cloud remote sensing data centre unit (CLU). Generated by the cloud profiling unit of the ACTRIS Data Centre. Available at https://hdl.handle.net/21.12132/2. 7a5d559b30c54be1. Accessed August 17, 2023.
- Ghahreman, R, Gong, W, Galí, M, Norman, AL, Beagley, SR, Akingunola, A, Zheng, Q, Lupu, A, Lizotte, M, Levasseur, M, Leaitch, WR. 2019. Dimethyl sulfide and its role in aerosol formation and growth in the Arctic summer—A modelling study. *Atmospheric Chemistry and Physics* 19(23): 14455–14476. DOI: http://dx.doi.org/10.5194/acp-19-14455-2019.
- **Heintzenberg, J, Leck, C.** 2012. The summer aerosol in the central Arctic 1991–2008: Did it change or not? *Atmospheric Chemistry and Physics* **12**(9): 3969–3983. DOI: http://dx.doi.org/10.5194/acp-12-3969-2012.
- **Heintzenberg, J, Leck, C, Tunved, P.** 2015. Potential source regions and processes of aerosol in the summer Arctic. *Atmospheric Chemistry and Physics* **15**(11): 6487–6502. DOI: http://dx.doi.org/10. 5194/acp-15-6487-2015.
- **Held, A, Brooks, IM, Leck, C, Tjernström, M.** 2011. On the potential contribution of open lead particle emissions to the central Arctic aerosol concentration. *Atmospheric Chemistry and Physics* **11**(7): 3093–3105. DOI: http://dx.doi.org/10.5194/acp-11-3093-2011.
- Hoppel, WA, Frick, GM, Fitzgerald, JW, Larsen, RE. 1994. Marine boundary layer measurements of new particle formation and the effects nonprecipitating clouds have on aerosol size distribution. *Journal of Geophysical Research* **99**(D7): 14443–14459. DOI: http://dx.doi.org/10.1029/94JD00797.
- **Igel, AL, Ekman, AML, Leck, C, Tjernström, M, Savre, J, Sedlar, J.** 2017. The free troposphere as a potential source of Arctic boundary layer aerosol particles. *Geophysical Research Letters* **44**(13): 7053–7060. DOI: http://dx.doi.org/10.1002/2017GL073808.
- Karlsson, L, Baccarini, A, Duplessis, P, Baumgardner, D, Brooks, IM, Chang, RYW, Dada, L, Dällenbach, KR, Heikkinen, L, Krejci, R, Leaitch, WR, Leck, C, Partridge, DG, Salter, ME, Wernli, H, Wheeler, MJ, Schmale, J, Zieger, P. 2022. Physical and chemical properties of cloud droplet residuals and aerosol particles during the Arctic Ocean 2018 expedition. *Journal of Geophysical Research: Atmospheres* 127(11): e2021JD036383. DOI: http://dx.doi.org/10.1029/2021JD036383.

- Karlsson, L, Krejci, R, Koike, M, Ebell, K, Zieger, P. 2021. A long-term study of cloud residuals from low-level Arctic clouds. *Atmospheric Chemistry and Physics* **21**(11): 8933–8959. DOI: http://dx.doi.org/10.5194/acp-21-8933-2021.
- Kecorius, S, Vogl, T, Paasonen, P, Lampilahti, J, Rothenberg, D, Wex, H, Zeppenfeld, S, van Pinxteren, M, Hartmann, M, Henning, S, Gong, X, Welti, A, Kulmala, M, Stratmann, F, Herrmann, H, Wiedensohler, A. 2019. New particle formation and its effect on cloud condensation nuclei abundance in the summer Arctic: A case study in the fram strait and barents sea. *Atmospheric Chemistry and Physics* 19(22): 14339–14364. DOI: http://dx.doi.org/10.5194/acp-19-14339-2019.
- **Knust, R.** 2017. Polar research and supply vessel POLAR-STERN operated by the Alfred-Wegener-Institute. *Journal of large-scale research facilities JLSRF* **3**: A119. DOI: http://dx.doi.org/10.17815/jlsrf-3-163.
- Kulmala, M, Vehkamäki, H, Petäjä, T, Dal Maso, M, Lauri, A, Kerminen, VM, Birmili, W, McMurry, PH. 2004. Formation and growth rates of ultrafine atmospheric particles: A review of observations. *Journal of Aerosol Science* **35**(2): 143–176. DOI: http://dx.doi.org/10.1016/j.jaerosci.2003.10.003.
- Kupiszewski, P, Leck, C, Tjernström, M, Sjogren, S, Sedlar, J, Graus, M, Müller, M, Brooks, B, Swietlicki, E, Norris, S, Hansel, A. 2013. Vertical profiling of aerosol particles and trace gases over the central Arctic Ocean during summer. *Atmospheric Chemistry and Physics* 13(24): 12405–12431. DOI: http://dx.doi.org/10.5194/acp-13-12405-2013.
- Lawler, MJ, Saltzman, ES, Karlsson, L, Zieger, P, Salter, M, Baccarini, A, Schmale, J, Leck, C. 2021. New insights into the composition and origins of ultrafine aerosol in the summertime high Arctic. *Geophysical Research Letters* 48(21): e2021GL094395. DOI: http://dx.doi.org/10.1029/2021GL094395.
- Leaitch, WR, Korolev, A, Aliabadi, AA, Burkart, J, Willis, MD, Abbatt, JPD, Bozem, H, Hoor, P, Köllner, F, Schneider, J, Herber, A, Konrad, C, Brauner, R. 2016. Effects of 20–100 nm particles on liquid clouds in the clean summertime Arctic. *Atmospheric Chemistry and Physics* 16(17): 11107–11124. DOI: http://dx.doi.org/10.5194/acp-16-11107-2016.
- **Loewe, K, Ekman, AML, Paukert, M, Sedlar, J, Tjernström, M, Hoose, C.** 2017. Modelling micro- and macrophysical contributors to the dissipation of an Arctic mixed-phase cloud during the Arctic Summer Cloud Ocean Study (ASCOS). *Atmospheric Chemistry and Physics* **17**(11): 6693–6704. DOI: http://dx.doi.org/10.5194/acp-17-6693-2017.
- Lonardi, M, Akansu, EF, Ehrlich, A, Mazzola, M, Pilz, C, Shupe, MD, Siebert, H, Wendisch, M. 2023. Tethered balloon-borne observations of thermal-infrared irradiance and cooling rate profiles in the Arctic atmospheric boundary layer. *EGUsphere* **2023**: 1–26. DOI: http://dx.doi.org/10.5194/egusphere-2023-1396.

- Lonardi, M, Pilz, C, Akansu, EF, Dahlke, S, Egerer, U, Ehrlich, A, Griesche, H, Heymsfield, AJ, Kirbus, B, Schmitt, CG, Shupe, MD, Siebert, H, Wehner, B, Wendisch, M. 2022a. Tethered balloon-borne profile measurements of atmospheric properties in the cloudy atmospheric boundary layer over the Arctic sea ice during MOSAiC: Overview and first results. *Elementa: Science of the Anthropocene* 10(1): 000120. DOI: http://dx.doi.org/10.1525/ELEMEN TA.2021.000120.
- Lonardi, M, Pilz, C, Siebert, H, Ehrlich, A, Wendisch, M. 2022b. Tethered balloon-borne measurements of terrestrial radiation during MOSAiC leg 4 in July 2020. PANGAEA. DOI: http://dx.doi.org/10.1594/PANGAEA.944200.
- **Lubin, D, Vogelmann, AM.** 2006. A climatologically significant aerosol longwave indirect effect in the Arctic. *Nature* **439**(7075): 453–456. DOI: http://dx.doi.org/10.1038/nature04449.
- Maturilli, M, Sommer, M, Holdridge, DJ, Dahlke, S, Graeser, J, Sommerfeld, A, Jaiser, R, Deckelmann, H, Schulz, A. 2022. MOSAiC radiosonde data (level 3). PANGAEA. DOI: http://dx.doi.org/10.1594/PANGAEA.943870.
- Mauritsen, T, Sedlar, J, Tjernström, M, Leck, C, Martin, M, Shupe, M, Sjogren, S, Sierau, B, Persson, POG, Brooks, IM, Swietlicki, E. 2011. An Arctic CCN-limited cloud-aerosol regime. *Atmospheric Chemistry and Physics* 11(1): 165–173. DOI: http://dx.doi.org/10.5194/acp-11-165-2011.
- Morris, V, Ermold, B. 2022. Ceilometer (CEIL10M). Atmospheric Radiation Measurement (ARM) User Facility. DOI: http://dx.doi.org/10.5439/1497398.
- Morrison, H, De Boer, G, Feingold, G, Harrington, J, Shupe, MD, Sulia, K. 2012. Resilience of persistent Arctic mixed-phase clouds. *Nature Geoscience* **5**(1): 11–17. DOI: http://dx.doi.org/10.1038/ngeo1332.
- Mungall, EL, Abbatt, JPD, Wentzell, JJB, Lee, AKY, Thomas, JL, Blais, M, Gosselin, M, Miller, LA, Papakyriakou, T, Willis, MD, Liggio, J. 2017. Microlayer source of oxygenated volatile organic compounds in the summertime marine Arctic boundary layer. *Proceedings of the National Academy of Sciences* 114(24): 6203–6208. DOI: http://dx.doi.org/10.1073/pnas.1620571114.
- Nixdorf, U, Dethloff, K, Rex, M, Shupe, M, Sommerfeld, A, Perovich, DK, Nicolaus, M, Heuzé, C, Rabe, B, Loose, B, Damm, E, Gradinger, R, Fong, A, Maslowski, W, Rinke, A, Kwok, R, Spreen, G, Wendisch, M, Herber, A, Hirsekorn, M, Mohaupt, V, Frickenhaus, S, Immerz, A, Weiss-Tuider, K, König, B, Mengedoht, D, Regnery, J, Gerchow, P, Ransby, D, Krumpen, T, Morgenstern, A, Haas, C, Kanzow, T, Rack, FR, Saitzev, V, Sokolov, V, Makarov, A, Schwarze, S, Wunderlich, T, Wurr, K, Boetius, A. 2021. MOSAiC extended acknowledgement. Available at https://zenodo.org/record/5541624. Accessed August 17, 2023.
- Overland, J, Francis, JA, Hall, R, Hanna, E, Kim, SJ, Vihma, T. 2015. The melting Arctic and midlatitude

- weather patterns: Are they connected? *Journal of Climate* **28**(20): 7917–7932. DOI: http://dx.doi. org/10.1175/JCLI-D-14-00822.1.
- Pilz, C, Düsing, S, Wehner, B, Müller, T, Siebert, H, Voigtländer, J, Lonardi, M. 2022a. CAMP: An instrumented platform for balloon-borne aerosol particle studies in the lower atmosphere. Atmospheric Measurement Techniques 15(23): 6889–6905. DOI: http://dx.doi.org/10.5194/amt-15-6889-2022.
- Pilz, C, Lonardi, M, Egerer, U, Siebert, H, Ehrlich, A, Heymsfield, AJ, Schmitt, CG, Shupe, MD, Wehner, B, Wendisch, M. 2023. Profile observations of the Arctic atmospheric boundary layer with the BELUGA tethered balloon during MOSAiC. *Nature Scientific Data* 10(1): 1–12. DOI: http://dx.doi.org/10.1038/s41597-023-02423-5.
- **Pilz, C, Lonardi, M, Siebert, H, Wehner, B.** 2022b. Tethered balloon-borne measurements of aerosol particle microphysics during the MOSAiC expedition from June to July 2020. Leipzig, Germany: Leibniz-Institut für Troposphärenforschung e.V., PANGAEA. DOI: http://dx.doi.org/10.1594/PANGAEA.943907.
- **Pilz, C, Siebert, H, Lonardi, M.** 2022c. Tethered balloon-borne measurements of meteorological parameters during MOSAiC leg 4 in June and July 2020. PAN-GAEA. DOI: http://dx.doi.org/10.1594/PANGAEA. 952341.
- Price, R, Baccarini, A, Schmale, J, Zieger, P, Brooks, IM, Field, P, Carslaw, KS. 2023. Late summer transition from a free-tropospheric to boundary layer source of Aitken mode aerosol in the high Arctic. *Atmospheric Chemistry and Physics* **23**(5): 2927–2961. DOI: http://dx.doi.org/10.5194/acp-23-2927-2023.
- Rantanen, M, Karpechko, AY, Lipponen, A, Nordling, K, Hyvärinen, O, Ruosteenoja, K, Vihma, T, Laaksonen, A. 2022. The Arctic has warmed nearly four times faster than the globe since 1979. *Communications Earth & Environment* **3**(1): 1–10. DOI: http://dx.doi.org/10.1038/s43247-022-00498-3.
- Rinke, A, Knudsen, EM, Mewes, D, Dorn, W, Handorf, D, Dethloff, K, Moore, JC. 2019. Arctic summer sea ice melt and related atmospheric conditions in coupled regional climate model simulations and observations. *Journal of Geophysical Research: Atmospheres* **124**(12): 6027–6039. DOI: http://dx.doi.org/10.1029/2018JD030207.
- **Schmale, J, Baccarini, A.** 2021. Progress in unraveling atmospheric new particle formation and growth across the Arctic. *Geophysical Research Letters* **48**(14): e2021GL094198. DOI: http://dx.doi.org/10.1029/2021GL094198.
- **Sedlar, J, Shupe, MD, Tjernström, M.** 2012. On the relationship between thermodynamic structure and cloud top, and its climate significance in the Arctic. *Journal of Climate* **25**(7): 2374–2393. DOI: http://dx.doi.org/10.1175/JCLI-D-11-00186.1.
- **Serreze, MC**, **Barry, RG**. 2011. Processes and impacts of Arctic amplification: A research synthesis. *Global*

- and Planetary Change **77**(1–2): 85–96. DOI: http://dx.doi.org/10.1016/j.gloplacha.2011.03.004.
- **Shupe, MD, Intrieri, JM.** 2004. Cloud radiative forcing of the Arctic surface: The influence of cloud properties, surface albedo, and solar zenith angle. *Journal of Climate* **17**(3): 616–628. DOI: http://dx.doi.org/10. 1175/1520-0442(2004)017<0616:CRFOTA>2.0. CO:2.
- Shupe, MD, Persson, POG, Brooks, IM, Tjernström, M, Sedlar, J, Mauritsen, T, Sjogren, S, Leck, C. 2013. Cloud and boundary layer interactions over the Arctic sea ice in late summer. *Atmospheric Chemistry and Physics* **13**(18): 9379–9399. DOI: http://dx.doi.org/10.5194/acp-13-9379-2013.
- Shupe, MD, Rex, M, Blomquist, B, Persson, POG, Schmale, J. Uttal, T. Althausen, D. Angot, H. Archer, S, Bariteau, L, Beck, I, Bilberry, J, Bucci, S. Buck, C. Boyer, M. Brasseur, Z. Brooks, IM, Calmer, R, Cassano, J, Castro, V, Chu, D, Costa, D, Cox, CJ, Creamean, J, Crewell, S, Dahlke, S, Damm, E, de Boer, G, Deckelmann, H, Dethloff, K, Dütsch, M, Ebell, K, Ehrlich, A, Ellis, J, Engelmann, R, Fong, AA, Frey, MM, Gallagher, MR, Ganzeveld, L. Gradinger, R. Graeser, J. Greenamyer, V, Griesche, H, Griffiths, S, Hamilton, J, Heinemann, G. Helmig, D. Herber, A. Heuzé, C. Hofer, J, Houchens, T, Howard, D, Inoue, J, Jacobi, HW, Jaiser, R, Jokinen, T, Jourdan, O, Jozef, G, King, W, Kirchgaessner, A, Klingebiel, M, Krassovski, M, Krumpen, T, Lampert, A, Landing, W, Laurila, T, Lawrence, D, Lonardi, M, Loose, B, Lüpkes, C, Maahn, M, Macke, A, Maslowski, W. Marsay, C. Maturilli, M. Mech, M, Morris, S, Moser, M, Nicolaus, M, Ortega, P, Osborn, J, Pätzold, F, Perovich, DK, Petäjä, T, Pilz, C, Pirazzini, R, Posman, K, Powers, H, Pratt, KA, Preußer, A. Quéléver, L. Radenz, M. Rabe, B. Rinke, A. Sachs, T. Schulz, A. Siebert, H. Silva, T. Solomon, A, Sommerfeld, A, Spreen, G, Stephens, M, Stohl, A, Svensson, G, Uin, J, Viegas, J. Voigt, C. von der Gathen, P. Wehner, B. Welker, JM, Wendisch, M, Werner, M, Xie, Z, Yue, F. 2022. Overview of the MOSAiC expedition: Atmosphere. Elementa: Science of the Anthropocene 10(1). 00060. DOI: http://dx.doi.org/10.1525/ ELEMENTA.2021.00060.
- Solomon, A, Shupe, MD, Persson, POG, Morrison, H. 2011. Moisture and dynamical interactions maintaining decoupled Arctic mixed-phase stratocumulus in the presence of a humidity inversion. *Atmospheric Chemistry and Physics* **11**(19): 10127–10148. DOI: http://dx.doi.org/10.5194/acp-11-10127-2011.
- **Sprenger, M, Wernli, H.** 2015. The LAGRANTO Lagrangian analysis tool—Version 2.0. *Geoscientific Model Development* **8**(8): 2569–2586. DOI: http://dx.doi.org/10.5194/gmd-8-2569-2015.
- **Tjernström, M, Graversen, RG.** 2009. The vertical structure of the lower Arctic troposphere analysed from observations and the ERA-40 reanalysis. *Quarterly*

- *Journal of the Royal Meteorological Society* **135**(639): 431–443. DOI: http://dx.doi.org/10.1002/QJ.380.
- **Tjernström, M, Shupe, MD, Brooks, IM, Achtert, P, Prytherch, J, Sedlar, J.** 2019. Arctic summer airmass transformation, surface inversions, and the surface energy budget. *Journal of Climate* **32**(3): 769–789. DOI: http://dx.doi.org/10.1175/JCLI-D-18-0216.1.
- Wehner, B, Werner, F, Ditas, F, Shaw, RA, Kulmala, M, Siebert, H. 2015. Observations of new particle formation in enhanced UV irradiance zones near cumulus clouds. *Atmospheric Chemistry and Physics* **15**(20): 11701–11711. DOI: http://dx.doi.org/10.5194/acp-15-11701-2015.
- Wendisch, M. Brückner, M. Crewell, S. Ehrlich, A. Notholt, J. Lüpkes, C. Macke, A. Burrows, JP, Rinke, A, Quaas, J, Maturilli, M, Schemann, V, Shupe, MD, Akansu, EF, Barrientos-Velasco, C, Bärfuss, K, Blechschmidt, AM, Block, K, Bougoudis, I, Bozem, H, Böckmann, C, Bracher, A, Bresson, H, Bretschneider, L, Buschmann, M, Chechin, DG, Chylik, J, Dahlke, S, Deneke, H, Dethloff, K, Donth, T, Dorn, W, Dupuy, R, Ebell, K, Egerer, U, Engelmann, R, Eppers, O, Gerdes, R, Gierens, R. Gorodetskaya, IV, Gottschalk, M, Griesche, H., Gryanik, VM, Handorf, D, Harm-Altstädter, B, Hartmann, J, Hartmann, M, Heinold, B, Herber, A, Herrmann, H, Heygster, G, Höschel, I, Hofmann, Z, Hölemann, J, Hünerbein, A, Jafariserajehlou, S, Jäkel, E, Jacobi, C, Janout, M, Jansen, F, Jourdan, O, Jurányi, Z, Kalesse-Los, H, Kanzow, T, Käthner, R, Kliesch, LL, Klingebiel, M, Knudsen, EM, Kovács, T, Körtke, W, Krampe, D, Kretzschmar, J, Kreyling, D, Kulla, B, Kunkel, D, Lampert, A, Lauer, M, Lelli, L, von Lerber, A, Linke, O, Löhnert, U, Lonardi, M, Losa, SN, Losch, M, Maahn, M, Mech, M, Mei, L, Mertes, S, Metzner, E, Mewes, D, Michaelis, J, Mioche, G, Moser, M, Nakoudi, K, Neggers, R, Neuber, R, Nomokonova, T, Oelker, J, Papakonstantinou-Presvelou, I, Pätzold, F, Pefanis, V, Pohl, C, van Pinxteren, M, Radovan, A, Rhein, M, Rex, M, Richter, A, Risse, N, Ritter, C, Rostosky, P, Rozanov, VV, Ruiz Donoso, E, Saavedra Garfias, P, Salzmann, M, Schacht, J., Schäfer, M., Schneider, J., Schnierstein, N, Seifert, P, Seo, S, Siebert, H, Soppa, MA, Spreen, G, Stachlewska, IS, Stapf, J, Stratmann, F, Tegen, I, Viceto, C, Voigt, C, Vountas, M, Walbröl, A. Walter, M. Wehner, B. Wex, H. Willmes, S, Zanatta, M, Zeppenfeld, S. 2023a. Atmospheric and surface processes, and feedback mechanisms determining Arctic amplification: A review of first results and prospects of the (AC)³ project. Bulletin of the American Meteorological Society **104**(1): E208–E242. DOI: http://dx.doi.org/10. 1175/BAMS-D-21-0218.1.
- Wendisch M, Handorf D, Tegen I, Neggers RAJ, Spreen G. 2021. Glimpsing the ins and outs of the Arctic atmospheric cauldron. *Eos* 102. DOI: http://dx.doi.org/10.1029/2021EO155959.

- Wendisch, M, Macke, A, Ehrlich, A, Lüpkes, C, Mech, M, Chechin, D, Dethloff, K, Velasco, CB, Bozem, H, Brückner, M, Clemen, HC, Crewell, S, Donth, T, Dupuy, R, Ebell, K, Egerer, U, Engelmann, R, Engler, C. Eppers, O. Gehrmann, M. Gong, X. Gottschalk, M. Gourbeyre, C. Griesche, H. Hartmann, J. Hartmann, M. Heinold, B. Herber, A. Herrmann, H, Heygster, G, Hoor, P, Jafariserajehlou, S, Jäkel, E, Järvinen, E, Jourdan, O, Kästner, U. Kecorius, S. Knudsen, EM, Köllner, F. Kretzschmar, J. Lelli, L. Leroy, D. Maturilli, M. Mei, L, Mertes, S, Mioche, G, Neuber, R, Nicolaus, M, Nomokonova, T, Notholt, J, Palm, M, van Pinxteren, M. Quaas, J. Richter, P. Ruiz-Donoso, E. Schäfer, M, Schmieder, K, Schnaiter, M, Schneider, J., Schwarzenböck, A., Seifert, P., Shupe, MD, Siebert, H., Spreen, G., Stapf, J., Stratmann, F., Vogl, T, Welti, A, Wex, H, Wiedensohler, A, Zanatta, M, **Zeppenfeld, S**. 2019. The Arctic cloud puzzle using ACLOUD/PASCAL multiplatform observations to unravel the role of clouds and aerosol particles in Arctic amplification. Bulletin of the American Meteorological Society **100**(5): 841–871. DOI: http://dx. doi.org/10.1175/BAMS-D-18-0072.1.
- Wendisch, M, Stapf, J, Becker, S, Ehrlich, A, Jäkel, E, Klingebiel, M, Lüpkes, C, Schäfer, M, Shupe, MD. 2023b. Effects of variable ice—ocean surface properties and air mass transformation on the Arctic radiative energy budget. *Atmospheric Chemistry and Physics* **23**(17): 9647–9667. DOI: http://dx.doi.org/10.5194/acp-23-9647-2023.
- Williams, AS, Igel, AL. 2021. Cloud top radiative cooling rate drives non-precipitating stratiform cloud responses to aerosol concentration. *Geophysical Research Letters* **48**(18): e2021GL094740. DOI: http://dx.doi.org/10.1029/2021GL094740.
- Willis, MD, Bozem, H, Kunkel, D, Lee, AKY, Schulz, H, Burkart, J, Aliabadi, AA, Herber, AB, Leaitch, WR, Abbatt, JPD. 2019. Aircraft-based measurements of high Arctic springtime aerosol show evidence for vertically varying sources, transport and composition. *Atmospheric Chemistry and Physics* **19**(1): 57–76. DOI: http://dx.doi.org/10.5194/acp-19-57-2019.
- Willis, MD, Burkart, J, Thomas, JL, Köllner, F, Schneider, J, Bozem, H, Hoor, PM, Aliabadi, AA, Schulz, H, Herber, AB, Leaitch, WR, Abbatt, JPD. 2016. Growth of nucleation mode particles in the summertime Arctic: A case study. *Atmospheric Chemistry and Physics* **16**(12): 7663–7679. DOI: http://dx.doi.org/10.5194/acp-16-7663-2016.
- Willis, MD, Köllner, F, Burkart, J, Bozem, H, Thomas, JL, Schneider, J, Aliabadi, AA, Hoor, PM, Schulz, H, Herber, AB, Leaitch, WR, Abbatt, JPD. 2017. Evidence for marine biogenic influence on summertime Arctic aerosol. *Geophysical Research Letters* **44**(12): 6460–6470. DOI: http://dx.doi.org/10. 1002/2017GL073359.
- Wohl, C, Li, Q, Cuevas, CA, Fernandez, RP, Yang, M, Saiz-Lopez, A, Simó, R. 2023. Marine biogenic emissions of benzene and toluene and their

contribution to secondary organic aerosols over the polar oceans. *Science Advances* **9**(4): eadd9031. DOI: http://dx.doi.org/10.1126/sciadv.add9031.

Zieger, P, Väisänen, O, Corbin, JC, Partridge, DG, Bastelberger, S, Mousavi-Fard, M, Rosati, B, Gysel,

M, Krieger, UK, Leck, C, Nenes, A, Riipinen, I, Virtanen, A, Salte, ME. 2017. Revising the hygroscopicity of inorganic sea salt particles. *Nature Communications* **8**(1): 1–10. DOI: http://dx.doi.org/10. 1038/ncomms15883.

How to cite this article: Pilz, C, Cassano, JJ, de Boer, G, Kirbus, B, Lonardi, M, Pöhlker, M, Shupe, MD, Siebert, H, Wendisch, M, Wehner, B. 2024. Tethered balloon measurements reveal enhanced aerosol occurrence aloft interacting with Arctic low-level clouds. *Elementa: Science of the Anthropocene* 12(1). DOI: https://doi.org/10.1525/elementa.2023.00120

Domain Editor-in-Chief: Detlev Helmig, Boulder AIR LLC, Boulder, CO, USA

Guest Editor: MingXi Yang, Plymouth Marine Laboratory, Plymouth, UK

Knowledge Domain: Atmospheric Science

Part of an Elementa Special Feature: The Multidisciplinary Drifting Observatory for the Study of Arctic Climate (MOSAiC)

Published: May 15, 2024 Accepted: March 18, 2024 Submitted: September 28, 2023

Copyright: © 2024 The Author(s). This is an open-access article distributed under the terms of the Creative Commons Attribution 4.0 International License (CC-BY 4.0), which permits unrestricted use, distribution, and reproduction in any medium, provided the original author and source are credited. See http://creativecommons.org/licenses/by/4.0/.

